International Journal of Solids and Structures 48 (2011) 1191–1209

Contents lists available at ScienceDirect

International Journal of Solids and Structures

journal homepage: www.elsevier.com/locate/ijsolstr

Discrete simulations of shear zone patterning in sand in earth pressure problems of a retaining wall

Ł. Widuliński [a], J. Tejchman [a,*], J. Kozicki [a], D. Leśniewska [b]

[a] Faculty of Civil and Environmental Engineering, Gdańsk University of Technology, Gdańsk, Poland
[b] Institute of Hydro-Engineering, Polish Academy of Sciences in Gdańsk and Koszalin Technical University, Poland

ARTICLE INFO

Article history:
Received 11 May 2010
Received in revised form 30 December 2010
Available online 13 January 2011

Keywords:
Earth pressure
Granular material
Discrete element method
Finite element method
Micro-polar hypoplasticity
Retaining wall
Rolling resistance
Shear zone

ABSTRACT

The intention of the paper is to check the capability of a discrete element method (DEM) to simulate a pattern of quasi-static shear zones in initially dense sand. Discrete calculations were carried out with a rigid and very rough retaining wall, undergoing passive and active horizontal translation, rotation about the top and rotation about the toe. To simulate the behavior of sand, the three-dimensional spherical discrete model was used allowing for grain rolling resistance. The geometry of calculated shear zones was qualitatively compared with experimental results of laboratory model tests using X-rays and Digital Image Correlation technique (DIC), and quantitatively with finite element results obtained with a micro-polar hypoplastic constitutive model. The results show that a discrete model is able to realistically predict the experimental pattern of shear zones in the sand interior. A satisfactory agreement with experiments and finite element calculations was achieved.

1. Introduction

Earth pressure on retaining walls is one of the soil mechanics classical problems. In spite of an intense theoretical and experimental research over more than 200 years, there are still large discrepancies between theoretical solutions and experimental results due to the complexity of the deformation field in granular bodies near the wall caused by localization of shear deformation (which is a fundamental phenomenon of granular material behavior, Roscoe, 1970; Vardoulakis, 1980; Tejchman and Gudehus, 2001; Gudehus and Nübel, 2004; Tejchman, 2008). It was experimentally observed (Vardoulakis, 1980; Han and Vardoulakis, 1991; Yoshida et al., 1995; Desrues and Viggiani, 2004) that localization can appear as single, multiple or pattern of shear zones, depending upon both initial and boundary conditions. It can be plane or curved. Within shear zones, pronounced grain rotations and curvatures connected to couple stresses, large strain gradients, and high void ratios together with material softening (negative second-order work) are expected. The thickness of shear zones depends on many various factors, as: the mean grain diameter, pressure level, initial void ratio, direction of deformation, grain roughness and grain size distribution (Tejchman, 2008). The knowledge of both the distribution of shear zones and distribution of shear and volumetric strains within shear zones is important to explain the mechanism of granular deformation. The multiple patterns of shear zones are not usually taken into account in engineering calculations.

Earth pressure on retaining walls is usually calculated within a theory of elasticity and plasticity. In plastic limit states, there are generally two approaches: static and kinematic. Within the first approach, assuming the material yielding behind the wall according to the Mohr–Coulomb law, one can obtain mathematically closed solutions of pressure distribution for simple boundary conditions (Caquot and Kerisel, 1948; Negre, 1959). In the case of complex boundary and load conditions, numerical solutions using a characteristics method for stress and velocity fields can be obtained (Sokolovski, 1965; Roscoe, 1970; James and Bransby, 1971; Szczepiński, 1974; Bransby and Milligan, 1975; Houlsby and Wroth, 1982; Milligan, 1983). Within a simpler kinematic approach, based on the force equilibrium, different failure mechanisms consisting of slip surfaces are assumed. From the equilibrium of forces acting on sliding rigid blocks, a resultant total earth pressure force can be calculated (Coulomb, 1773; Terzaghi, 1951; Gudehus, 1978). Theoretical solutions are very sensitive to the angle of internal friction of soil and soil-wall friction angle. They are not able to predict consistently deformations (Leśniewska and Mróz, 2001). Finite element calculations are more realistic than analytical solutions, since first, they take into account advanced constitutive laws describing the granular material behavior, and second, they can

* Corresponding author. Tel.: +48 58 347 1481; fax: +48 58 347 2044.
E-mail addresses: lwidul@pg.gda.pl (Ł. Widuliński), tejchmk@pg.gda.pl (J. Tejchman), jkozicki@pg.gda.pl (J. Kozicki), d.lesniewska@ibwpan.gda.pl (D. Leśniewska).

0020-7683/$ - see front matter © 2011 Elsevier Ltd. All rights reserved.
doi:10.1016/j.ijsolstr.2011.01.005

predict the evolution of localization of deformation. For FE-analyses of earth pressures in granular soils, a perfect plastic (Nakai, 1985), an elasto-plastic (Simpson and Wroth, 1972; Christian et al., 1977; Potts and Fourie, 1984), an elasto-plastic with remeshing (Hicks et al., 2001), a hypoplastic (Ziegler, 1986), and a micro-polar hypoplastic constitutive law (Tejchman and Dembicki, 2001; Nübel, 2002; Tejchman et al., 2007) were used. A characteristic length of micro-structure was not taken into account in the analyses except of calculations with a micro-polar hypoplastic law.

The intention of our paper is to check the capability of a discrete element model (DEM) to simulate a pattern of quasi-static shear zones in initially dense sand. The plane strain DEM calculations were carried out with sand placed behind a rigid and very rough retaining wall, undergoing passive and active movements: horizontal translation, rotation about the top and rotation about the toe. In a passive mode, a retaining wall moved towards the backfill and in an active mode away from it. To simulate the behavior of sand, the three-dimensional spherical discrete model YADE developed at University of Grenoble was used, allowing for introducing grain rolling resistance in order to take into account the grain roughness (Kozicki and Donze, 2008). The attention was laid on the influence of the different wall movement on the characteristic evolution of shear zones. The layout of calculated shear zones was qualitatively compared with corresponding experimental results of laboratory model tests performed by a number of researchers at University of Cambridge employing X-rays (Leśniewska, 2000) and also with some tests made by Niedostatkiewicz et al. (2010) – the latter were recorded using digital photography and subsequently analyzed by Digital Image Correlation (DIC). The experiments with X-rays and DIC were carried out with different sands, granular specimen sizes and initial void ratios. The discrete element (DE) results were also quantitatively compared with the finite element (FE) results obtained by modeling the sand behavior with a micro-polar hypoplastic constitutive model (Tejchman et al., 2007; Tejchman, 2008) for the same sand, its initial void ratio, specimen size and boundary conditions.

The capability of DEM to simulate a single shear zone during plane strain compression, direct and simple shearing was several times confirmed in the scientific literature (Iwashita and Oda, 1998; Thornton and Zhang, 2006; Pena et al., 2008; Ord et al., 2007; Luding, 2008). However, its capability to simulate complex patterns of shear zones in the interior of granulates has not been comprehensively checked yet. This paper is focused mainly on a direct comparison between finite and discrete results at the global level, i.e. with respect to patterns of shear zones and load–displacement diagrams. The comparative study of shear zones at the micro-level using these both different approaches will be published later.

2. Experimental shear zones

2.1. Shear zones recorded by X-rays

Comprehensive experimental studies on earth pressure problem in sand have been carried out at Cambridge University between 1962 and 1974. Two earth pressure apparatuses were employed. In case of the so called ‘small earth pressure apparatus’, the wall was 152 mm high and 152 mm wide (Arthur, 1962). In the remaining cases, the ‘large earth pressure apparatus’ was used, and the retaining wall was 330 mm high and 190 mm wide. The sand used was rounded coarse quartz “Leighton Buzzard” sand (grain size between 0.6 and 1.2 mm, mean grain diameter d_{50} = 0.9 mm) (Cabalar and Cevik, 2010). The evolution of shear localisation in sand was recorded using the radiographic technique

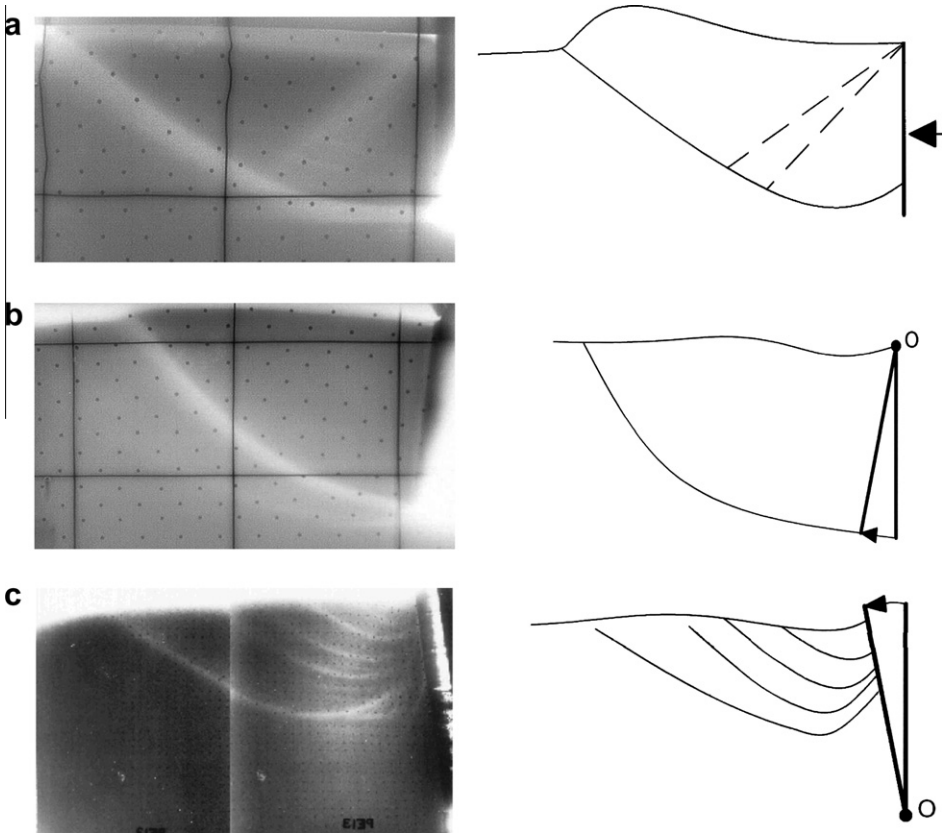

Fig. 1. Shear zones observed in experiments of passive mode with initially dense sand (radiographs and schematically): (a) during wall translation (Lucia, 1966), (b) during wall rotation around the top (Arthur, 1962) and (c) during wall rotation around the toe (Bransby, 1968) (*O* – rotation point) (radiographs from Leśniewska, 2000).

(Roscoe, 1970; Vardoulakis, 1980) which was able to directly detect a volume increase. Localized shear zones were detected in initially dense sands only. The Cambridge model tests were digitized and published by Leśniewska (2000).

Selected experimental patterns of cumulative density localization in initially dense sand recorded by X-ray technique during different wall movements are shown in Figs. 1 and 2. One distinct curved shear zone starting from the toe of the wall and accompanied by a weaker, secondary, wide radial shear zone propagating from the wall top were observed for a passively translating rigid wall (Fig. 1a). In the case of passive tests with a rigid wall rotating about its top, one distinct curved shear zone was observed in sand and also a trace of an accompanying weaker zone, starting from the same point (toe of the wall) and similar to the first one (Fig. 1b). Multiple parallel curved shear zones of a similar shape were observed during tests with a wall passively rotating about its toe (Fig. 1c). They started to emerge at the top of the wall and propagated towards the free boundary. For the active wall translation, one almost straight shear zone behind the wall occurred propagating from the wall toe (Fig. 2a) (Niedostatkiewicz, 2009). When a wall rotated around the top, a double curved zone was created (Fig. 2b). A family of nearly parallel straight zones extending between the wall and the specimen free boundary was found in the case of active tests with a wall rotating about its toe (Fig. 2c).

2.2. Shear zones visualized by Digital Image Correlation technique

Similar patterns of shear zones to the ones described in the previous section were obtained by applying a Digital Image Correlation technique (DIC) to digital photographs taken during recent small scale model tests on walls, which layout corresponded to the tests recorded by X-rays (Niedostatkiewicz et al., 2010). The model tests were carried out in a metal strong box 360 mm long, 220 mm high and 20 mm wide. Dry cohesionless so-called "Borowiec" sand with $d_{50} = 0.8$ mm and a uniformity coefficient $U = 5$ was used (Krasinski, 1998; Niedostatkiewicz, 2003).

DIC is an optical technique (White et al., 2003; Rechenmacher and Finno, 2004; Skarżynski et al., 2009) allowing to determine displacements on the basis of comparing successive pairs of digital photographs of a deforming specimen. The image intensity field assigns to each point in the image plane a scalar value, which reflects the light intensity of the corresponding point in the physical space. A so-called area of interest (AOI) is cut out of the digital image and divided into small sub-areas called interrogation cells (patches). If the deformation between two consecutive images is sufficiently small, the patterns of interrogation cells are supposed not to change their characteristics. A deformation pattern is determined by comparing two consecutive images captured by a camera which remains in a fixed position with its axis oriented perpendicular to

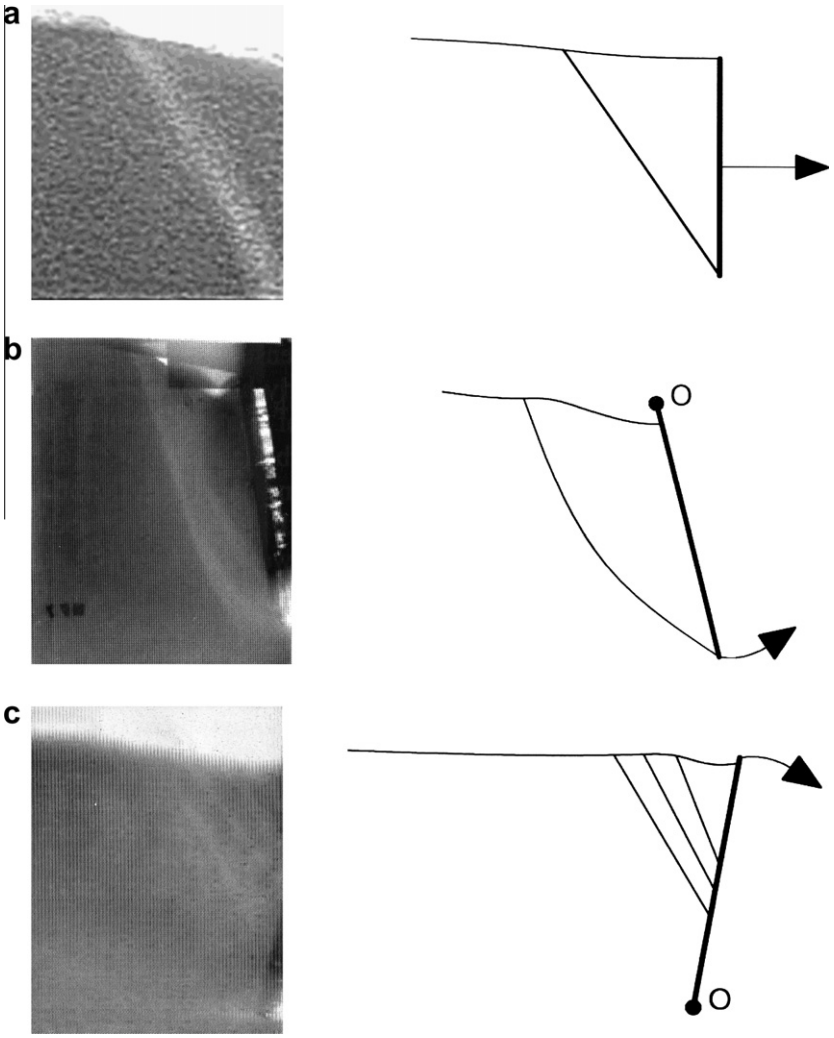

Fig. 2. Shear zones observed in experiments of active modes with initially dense sand (radiographs and schematically): (a) during wall translation (Niedostatkiewicz, 2009), (b) during wall rotation around top (Lord, 1969) and (c) during wall rotation around toe (Smith, 1972) (*O* – rotation point) (radiographs from Leśniewska, 2000).

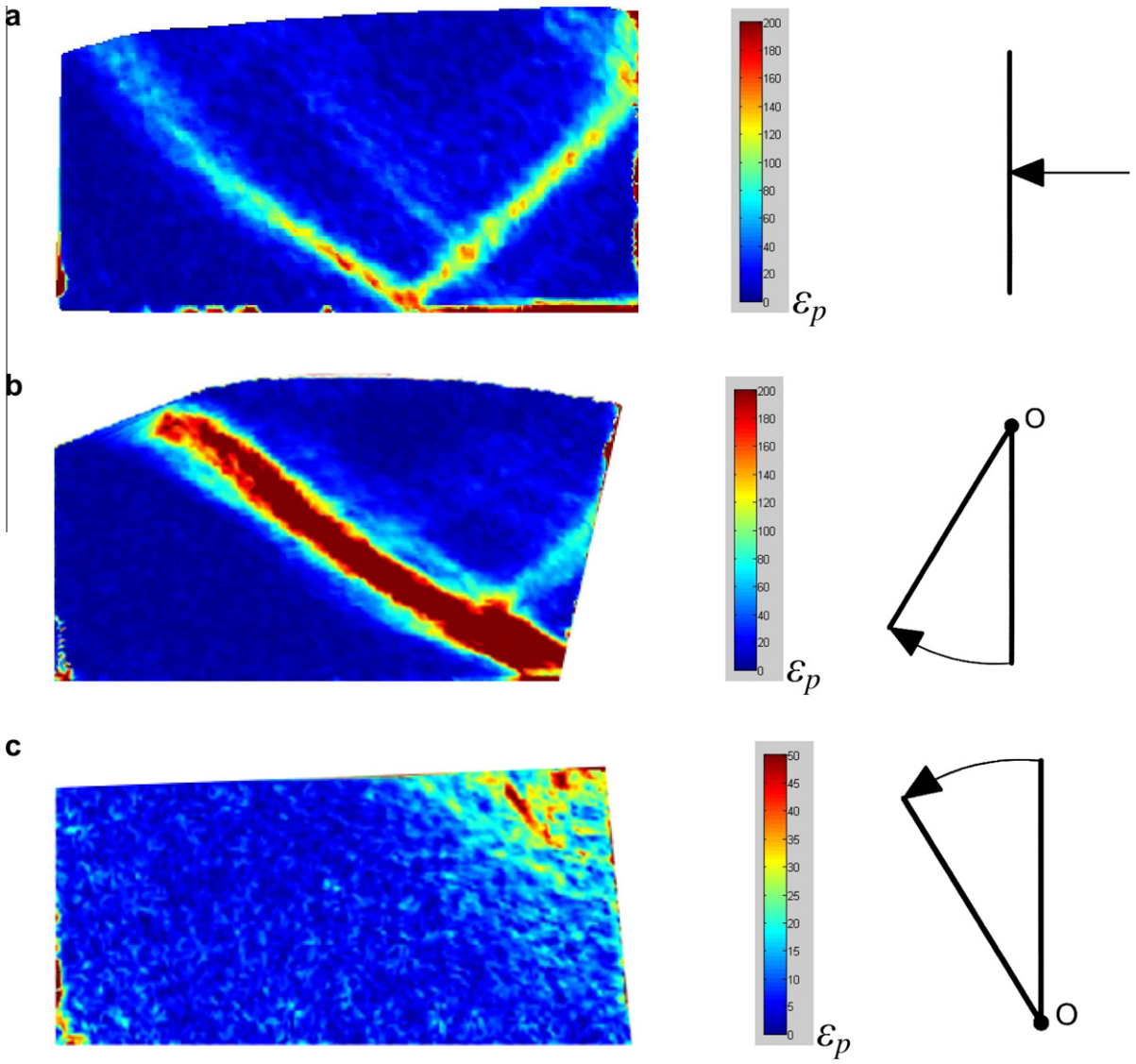

Fig. 3. Experimental distribution of deviatoric strain ε_p in initially dense sand (passive mode) from DIC (O – rotation point): (a) horizontal wall translation, (b) rotation about top and (c) rotation about toe (Niedostatkiewicz et al., 2010) (strain values are expressed by color scale).

the plane of deformation. To find a local displacement between images, a search zone is extracted from the second image. A correct local displacement vector for each interrogation cell is accomplished by means of a cross-correlation function, which calculates simply possible displacements by correlating all gray values from the first image with all gray values from the next image. The peak in the correlation function indicates that the two images are overlaying each other. The correlation operations are conducted in the frequency domain by taking the Fast Fourier Transform (FFT) of each patch. The procedure is continued by substituting a second image with a subsequent image. Thus, the evolution of displacements in the specimen can be captured. A direct DIC evaluation leads to an Eulerian description since the area of interest and the interrogation cell size are fixed. The relative displacements are next converted into a Lagrangian deformation field yielding total deformations with respect to the initial configuration. The accuracy of the DIC method for granular flow was discussed by White et al. (2003) and Słomiński et al. (2007).

Figs. 3 and 4 show the distribution of the resultant deviatoric strain ε_p on the basis of surface displacements of initially dense sand using DIC during passive (Fig. 3) and active (Fig. 4) wall movement. The strain values are expressed by a color scale attached to each figure[1]. The geometry of shear zones clearly resembles this obtained previously with X-rays (Figs. 1 and 2).

In the case of passive wall translation (Fig. 3a), two most distinct shear zones – a curvilinear one, connecting the toe of the wall with the specimen's free surface (it is the main shear zone which appears as the first one) and an accompanying radial shear zone are visible. In addition, two secondary (not fully developed) shear zones can be observed; one emerging slightly below the top of the wall in the right up corner of the sample and propagating to the free boundary, and the other one in the middle of the specimen, parallel to the main shear zone and propagating also to the free boundary (they appear slightly later as the first two shear zones).

For the passive wall rotation about its top (Fig. 3b), the main shear zone propagates from the toe of the wall up to the free boundary. It is initially horizontal along the bottom and later becomes inclined. In addition, two weaker secondary shear zones

[1] For interpretation of color in Figs. 3, 4, 8, 11, 14, 15 and 19, the reader is referred to the web version of this article.

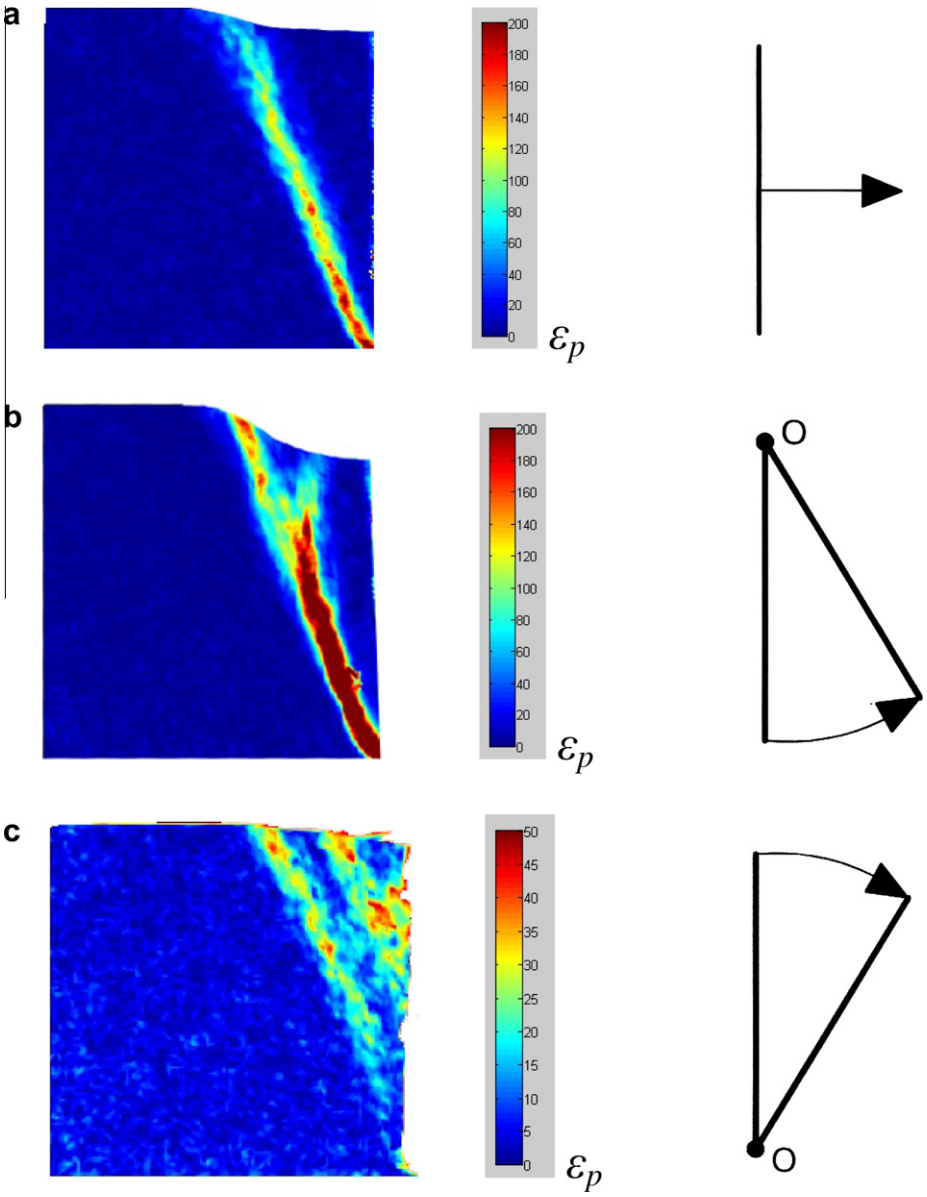

Fig. 4. Experimental distribution of deviatoric strain ε_p in initially dense sand (active mode) from DIC (O – rotation point): (a) horizontal wall translation, (b) rotation about top and (c) rotation about toe (Niedostatkiewicz et al., 2010) (strain values are expressed by color scale).

(one parallel and one perpendicular to the main inclined shear zone) start in the lower specimen region. When the wall rotates about its toe (passive mode, Fig. 3c), a family of curved, parallel shear zones can be distinguished in the right up corner of the specimen.

If the wall moves horizontally in an active mode (Fig. 4a), only one straight shear zone is created. When the wall rotates about its top (Fig. 4b), a curvilinear shear zone appears propagating from the toe of the wall up to the free boundary, but it splits later in the upper part of the sample. In the case of wall rotating about its top away from sand (Fig. 4c), two parallel zones emerge almost at the same time, crossed by the 'second family' lines.

3. Patterns of shear zones obtained in finite element calculations

The patterns of shear zones in "Karlsruhe sand" (Vardoulakis, 1980) (d_{50} = 0.50 mm, grain size among 0.08 mm and 1.8 mm, U = 2, maximum specific weight $\gamma_d^{max} = 17.4$ kN/m^3 and minimum specific weight $\gamma_d^{min} = 14.6$ kN/m^3) were calculated by the finite element method (FEM) using a micro-polar hypoplastic constitutive model (Tejchman et al., 2007; Tejchman, 2008; Tejchman and Górski, 2008) which was obtained by enhancement of a non-polar hypoplastic model (Bauer, 1996; Gudehus, 1996a) by introducing a characteristic length of microstructure according to the assumptions of a micro-polar theory.

A non-polar hypoplastic constitutive model describes the evolution of the effective stress tensor depending on the current void ratio, stress state and rate of deformation by isotropic non-linear tensorial functions according to a representation theorem by Wang (1970). The constitutive model was formulated by a heuristic process considering the essential mechanical properties of granular materials undergoing homogeneous deformations. A striking feature of hypoplasticity is that the shear rate is homogeneous of order 1 in the deformation rate. A hypoplastic model is capable of describing a number of significant properties of granular materials: non-linear stress–strain relationship, dilatant and contractant behavior, pressure dependence, density dependence

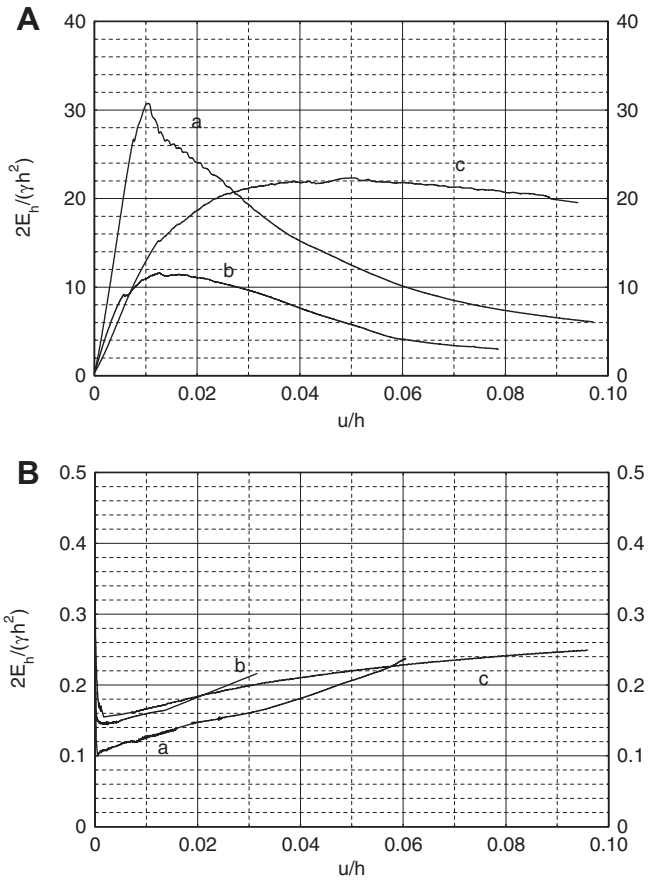

Fig. 5. Calculated resultant normalized horizontal earth pressure force $2E_h/(\gamma h^2)$ versus normalized horizontal wall displacement u/h from FEM: (A) passive case and (B) active case, (a) translating wall, (b) wall rotating around top, (c) wall rotating around bottom (E_h – horizontal earth pressure force, γ – density, h – wall height, u – horizontal wall displacement) (Tejchman, 2008).

and material softening. A further feature of hypoplastic models is the inclusion of critical states, i.e. states in which a grain aggregate can deform continuously at constant stress and constant volume. In contrast to elasto-plastic models, a decomposition of deformation components into elastic and plastic parts, the formulation of a yield surface, plastic potential, flow rule and hardening rule are not needed. Moreover, both the coaxiality (understood as a coincidence of the directions of the principal stresses and principal plastic strain increments) and stress-dilatancy rule are not assumed in advance (Tejchman and Wu, 2009). The hallmark of these models is their simple formulation and procedure for determining material parameters with standard laboratory experiments. The material parameters are related to granulometric properties, viz: size distribution, shape, angularity and hardness of grains (Herle and Gudehus, 1999). A further advantage lies in the fact that one single set of material parameters is valid for a wide range of pressures and densities. A hypoplastic constitutive model without a characteristic length can describe realistically the onset of shear localization, but not its further evolution. A characteristic length can be introduced into hypoplasticity by means of micro-polar, non-local or second-gradient theories (Tejchman, 2004). In this paper, a micro-polar theory was adopted (Mühlhaus, 1990). The micro-polar model makes use of rotations and couple stresses which have clear physical meaning for granular materials. The rotations can be observed during shearing, but remain negligible during homogeneous deformations (Oda, 1993). Pasternak and Mühlhaus (2001) have demonstrated that the additional rotational degree of freedom of a micro-polar continuum arises naturally by mathematical homogenization of an originally discrete system of spherical grains with contact forces and contact moments. A micro-polar continuum which is a continuous collection of particles behaving like rigid bodies combines two kinds of deformations at two different levels, viz: micro-rotation at the particle level and macro-deformation at the structural level. For the case of plane strain, each material point has three degrees of freedom: two translations and one independent rotation. The gradients of the rotation are related to the curvatures, which are associated with the couple stresses. The presence of the couple stresses gives rise to a non-symmetry of the stress tensor and to a characteristic length.

The constitutive relationship requires the following 10 material parameters: e_{i0}, e_{d0}, e_{c0}, ϕ_c, h_s, β, n, α, a_c and d_{50} (which are defined below). A precise calibration method of first eight material constants was given by Herle and Gudehus (1999). The compression parameters h_s and n are estimated from a single oedometric compression test with an initially loose specimen (h_s reflects the slope of the curve in a semi-logarithmic representation, and n its curvature). The constants α and β are found from a triaxial or plane strain test with a dense specimen and trigger the magnitude and position of the peak friction angle. The critical friction angle ϕ_c is determined from the angle of repose or measured in a triaxial test with a loose specimen. The values of e_{i0}, e_{d0}, e_{c0} (maximum, minimum and critical void ratio at pressure equal to zero) and d_{50} are obtained with conventional index tests ($e_{c0} \approx e_{max}, e_{d0} \approx e_{min}, e_{i0} \approx (1.1–1.5)e_{max}$). In turn, a micro-polar parameter a_c can be correlated with the grain roughness (Tejchman and Gudehus, 2001). It can be represented by a constant, e.g. $a_c = 1–5$, or connected to the parameter a_1^{-1}, e.g. $a_c = (0.5 - 1.5) \times a_1^{-1}$ (a_1 – parameter representing the deviatoric part of the normalized stress in critical states (Bauer, 1996)). The parameter a_1^{-1} lies in the range of 3.0–4.3 for usual critical friction angles between 25° and 35°. The FE-analyses were carried out with the material constants for the so-called Karlsruhe sand: $e_{i0} = 1.3$, $e_{d0} = 0.51$, $e_{c0} = 0.82$, $\phi_c = 30°$, $h_s = 190$ MPa, $\beta = 1$, $n = 0.5$, $a = 0.3$, $a_c = a_1^{-1}$ and $d_{50} = 0.5$ mm (Tejchman, 2008).

The plane strain FE calculations were performed with a Karlsruhe sand using a body of a height of $H = 200$ mm and length of $L = 400$ mm to simulate an earth pressure test with a passive translating wall by Gudehus and Schwing (1986) performed at Karlsruhe University (see also Nübel and Huang (2004)). Totally, 3200 triangular elements were used. The size of the quadrilaterals was $\leqslant 20 \times d_{50} = 10$ mm for $d_{50} = 0.5$ mm. The height of the retaining wall located at the right side of the sand body was assumed to be $h = 170$ mm ($h/H = 0.85$). The calculations were performed out with large deformations and curvatures (updated Lagrange formulation) by changing the element configuration and the element volume. The initial stresses were generated using a K_o-state without polar quantities: $\sigma_{22} = \gamma x_2$, $\sigma_{11} = \sigma_{33} = K_0 \gamma x_2$, $\sigma_{12} = \sigma_{21} = m_1 = m_2 = 0$ (σ_{11} – horizontal normal stress, σ_{22} – vertical normal stress, σ_{21} – horizontal shear stress, σ_{12} – vertical shear stress, m_1 – horizontal couple stress, m_2 – vertical couple stress, γ – initial volume weight of sand, x_2 – vertical coordinate measured from the top). The pressure coefficient at rest was assumed for dense sand as $K_0 = 0.47$ on the basis of a so-called element test for oedometric compression. Two sides and the bottom of the sand specimen were assumed to be very rough: $u_1 = 0$, $u_2 = 0$ and $\omega^c = 0$ (u_1 – horizontal displacement, u_2 – vertical displacement, ω^c – Cosserat rotation). The top of the sand specimen was traction and moment free. The retaining wall was assumed to be stiff and very rough ($u_2 = 0$ and $\omega^c = 0$). To prevent inadmissible stresses, a sub-stepping algorithm was used (deformations and curvature increments were divided into small parts within each step) (Tejchman, 2008). In addition, to avoid tensile stresses near the wall base, a significantly smaller

granular hardness was assumed there (h_s = 0.1 MPa). However, if tensile stresses were obtained in some elements, the stresses and couple stresses in these elements were replaced by values equal to zero.

The initial void ratio e_o was distributed non-uniformly in elements of the sand body by means of a random generator in such a way that the initial void ratio e_0 = 0.60 was increased in every element by the value $0.05 \times r (e_o = 0.60 + 0.05r)$, where r is a random number with a linear distribution within the range of (0.01, 0.99). Thus, each element of the sand specimen had a different initial void ratio at the beginning of deformation in the range between 0.60 and 0.65 (thus, the mean initial void ratio was e_o = 0.625).

The FE-results of a plane strain earth pressure problem for initially dense sand within a micro-polar continuum are shown in Figs. 5–7. Fig. 5 presents the evolution of the normalized horizontal earth pressure force $2E_h/(\gamma h^2)$ versus the normalized horizontal wall displacement u/h for three different wall movements (γ = 16.5 kN/m^3). In the case of a rotating wall, the horizontal displacement u is related to the wall displacement of the bottom point (wall rotating about the top) or top point (wall rotating around the bottom). In Figs. 5 and 6, the deformed meshes with the distribution of the void ratio and Cosserat rotation in the residual state are shown. The darker region indicates the higher void ratio. The Cosserat rotation is marked by circles with a diameter corresponding to the magnitude of the rotation in the given step.

The evolution of the passive horizontal earth pressure force $2E_h/(\gamma h^2)$ is similar in three cases (Fig. 5A). The horizontal force increases, reach a maximum for about u/h = 1–5%, next shows softening and tends to an asymptotic value. For the wall rotation around the bottom, a decrease of the curve after the peak is smaller (in the considered range of u/h). The maximum horizontal force on the wall is the highest for the wall translation, and the lowest for the wall rotation about the top. The maximum normalized horizontal earth pressure forces are high ($2E_h/\gamma h^2$ = 12–31) due to the high initial void ratio of sand, large wall roughness, high ratio between the mean grain diameter and wall height and low initial stress level. They are in the range of the usual (engineering) earth pressure coefficients (Gudehus, 1996b) determined under the assumption of one circular slip line (K_{pr} = 11.3–25.8) and three straight slip lines (K_{pt} = 13.4–23.7) at $\delta = \varphi^p$ = 40°–45° (δ – wall friction angle, φ^p – internal friction angle of dense sand at peak). However, the actual friction angles at peak φ^p in the shear zones are not known in advance (they depend strongly on the initial and boundary conditions of the entire system). Therefore, it is difficult to obtain realistic earth pressures with a conventional earth pressure theory. In addition (as the numerical calculations show), the different friction angles are mobilized in the various shear zones at the same time. The varying friction angles occur also along the same shear zone.

In the case of active earth pressure, the horizontal normalized forces drop sharply at the beginning of the wall movement, reach

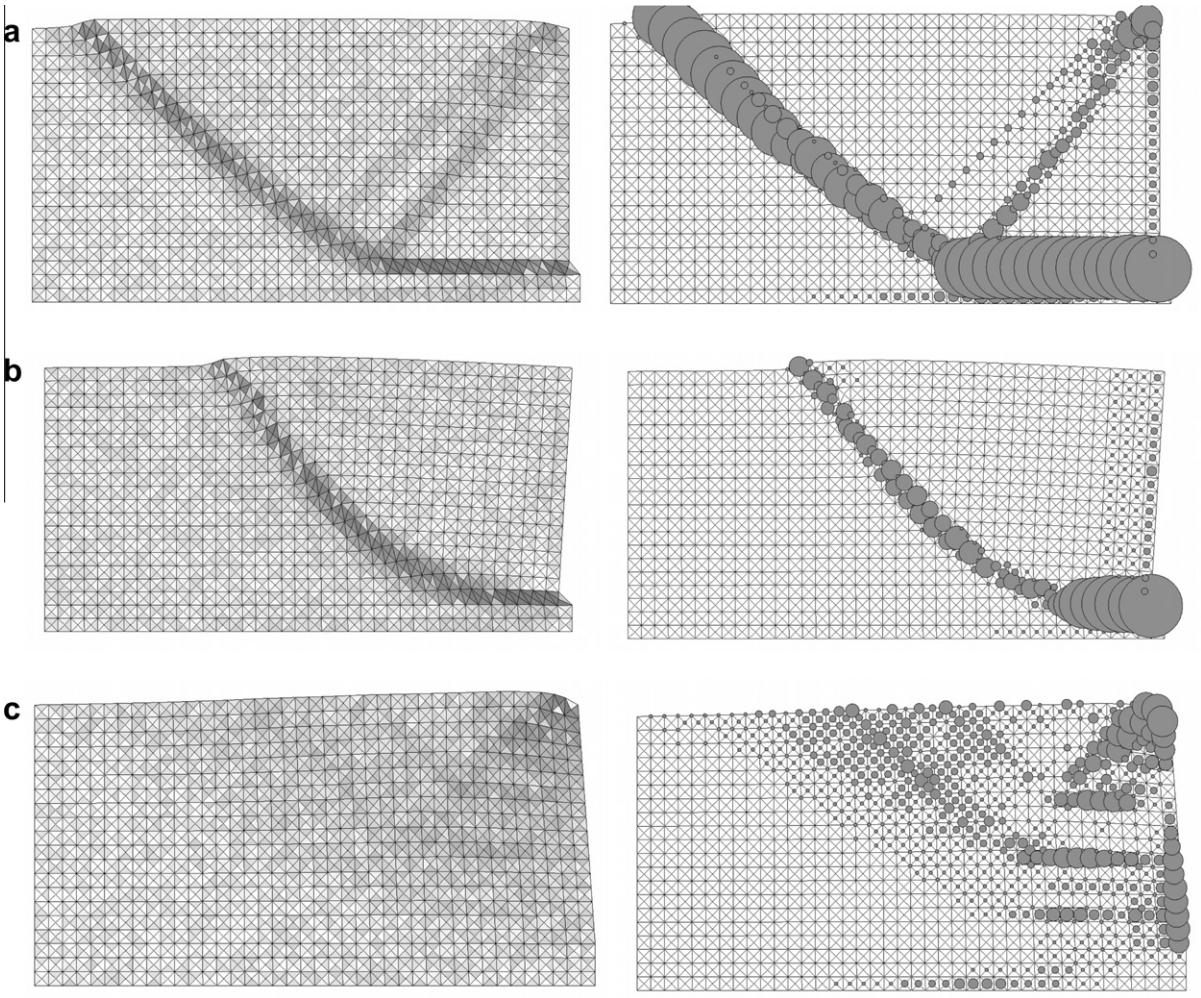

Fig. 6. Deformed FE-meshes with distribution of void ratio and Cosserat rotation at residual state for initially dense sand from FEM (passive case, u/h = 0.05): (a) translating wall, (b) wall rotating around toe and (c) wall rotating around top (Tejchman, 2008).

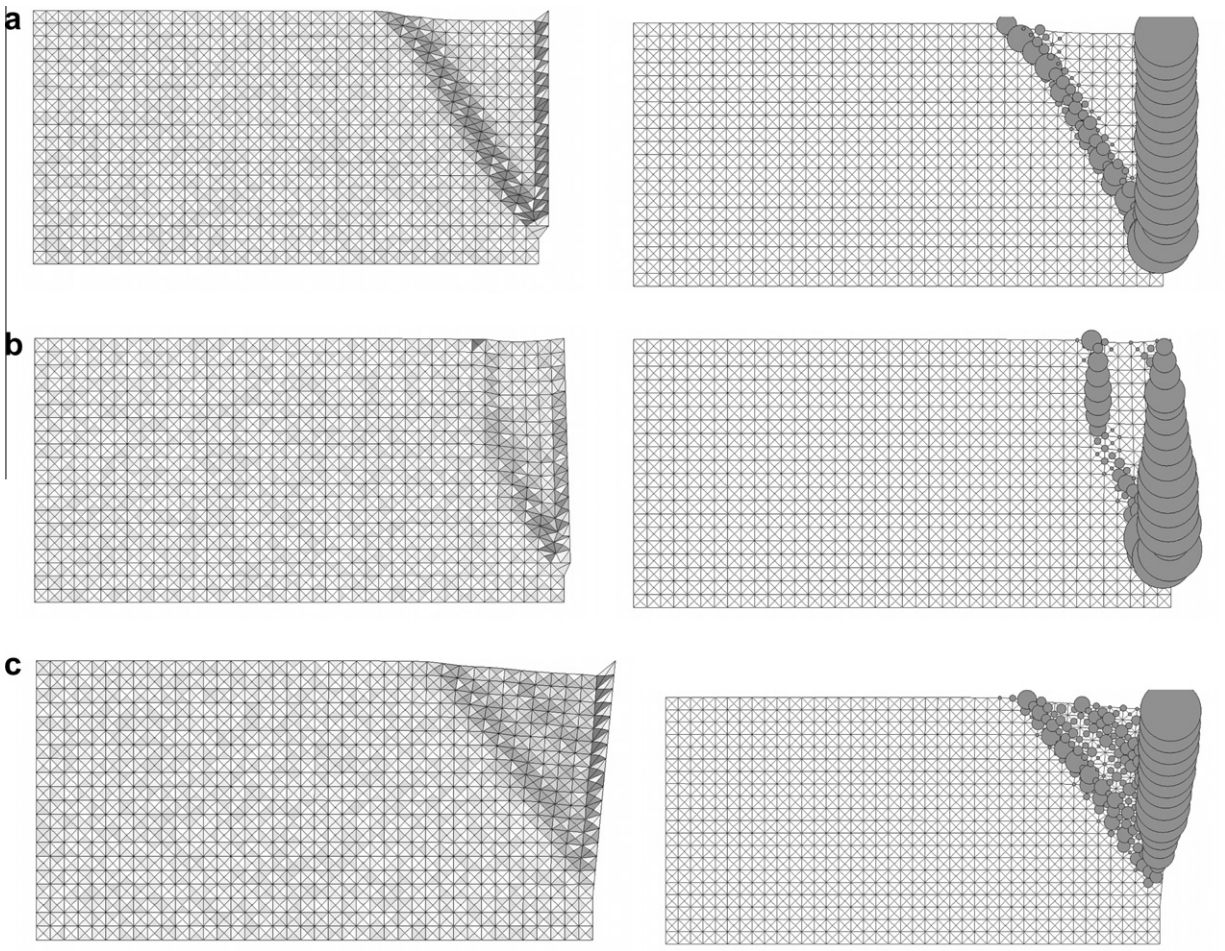

Fig. 7. Deformed FE-meshes with distribution of void ratio and Cosserat rotation at residual state for initially dense sand from FEM (active case, $u/h = 0.03–0.06$): (a) translating wall, (b) wall rotating around toe and (c) wall rotating around top (Tejchman, 2008).

the minimum at $u/h = 0.001–0.002$ and next increase continuously (Fig. 5B). The lowest earth pressure force occurs with the wall translation, and the largest with the wall rotation around the top. Thus, the relationship between the minimum active earth pressure and the type of the wall movement is inversed as compared to the maximum passive earth pressure and the type of the wall movement. The minimum normalized earth pressure forces ($2E_h/(\gamma h^2) = 0.10–0.16$) are slightly smaller than the usual earth pressure coefficients (Gudehus, 1996b) assuming a circular slip line ($K_a = 0.16–0.20$) or a straight slip line ($K_a = 0.14–0.16$) with $\delta = \varphi^p (\varphi^p = 40°–45°)$.

The geometry of shear zones, which are characterized in initially dense granulates by the appearance of Cosserat rotation and a strong increase of the void ratio, is very similar to those in experiments (Figs. 1–4). For the wall translation (Fig. 6a), five shear zones are obtained: one vertical along the very rough retaining wall, one zone projecting horizontally from the wall base, one inclined (slightly curved) zone spreading between the wall bottom and free boundary, and two radial oriented shear zones starting to form at the wall top (identically as in the test by Gudehus and Schwing (1986)). The inclined shear zone becomes dominant in the course of deformation. The second radial shear zone is not fully developed at $u/h = 0.07$. The maximum Cosserat rotation in the shear zones (at residual state) is about |15°|. In the case of the wall rotation about the top (Fig. 6b), only one curved shear zone occurs. When the retaining wall rotates

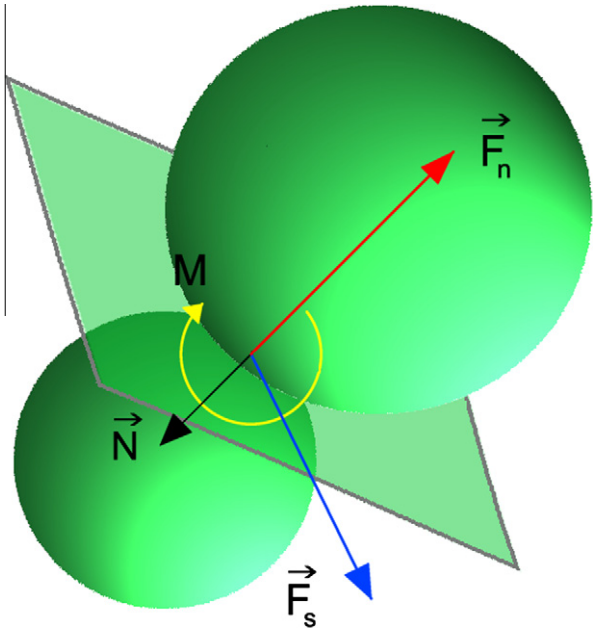

Fig. 8. Two spheres in contact ($\vec{F}_s$ – tangential contact force vector, $\vec{F}_n$ – normal contact force vector, $\vec{M}$ – contact moment vector, $\vec{N}$ - contact normal vector).

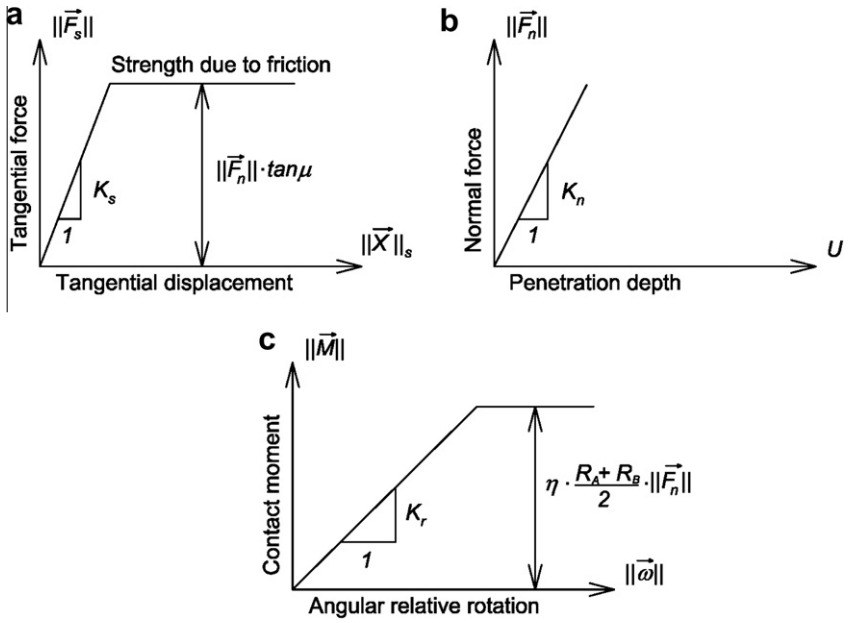

Fig. 9. Mechanical response of contact models: (a) tangential contact model, (b) normal contact model and (c) rolling contact model (Kozicki and Donze, 2008).

around the bottom (Fig. 6c), a pattern of curved parallel shear zones is obtained.

In the case of the active wall translation, two pronounced shear zones are obtained (Fig. 7a). A vertical one occurs along the wall, and the second one propagates from the wall bottom up to the free boundary. The internal shear zone is almost straight. When the wall rotates around the top, two shear zones are obtained again: the first along the wall and the second inside of sand starting from the wall bottom (Fig. 7b). The shear zone is strongly curved. In the case of a wall rotating around the bottom (Fig. 7c), three shear zones are obtained: one shear zone along the wall and two parallel internal shear zones.

The computation time was about 10 h on PC 2.0 GHz.

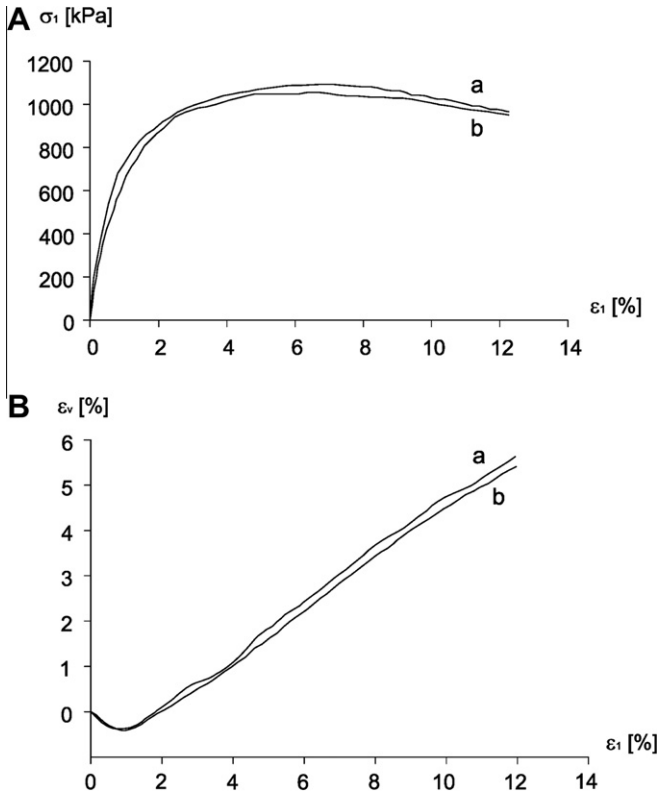

Fig. 10. Homogeneous triaxial test for granular specimen (to calibrate discrete material parameters): (A) vertical stress σ_1 versus vertical axial strain ε_1 and (B) volumetric strain ε_v versus vertical axial strain ε_1 ($p = 200$ kPa, $e_o = 0.53$, $d_{50} = 0.5$ mm): (a) experimental result (Wu, 1992), (b) discrete simulation ($E_c = 30$ GPa, $\upsilon_c = 0.3$, $\mu = 30°$, $\eta = 1.0$, $\beta = 0.15$) (Widuliński et al., 2009).

4. Discrete element method

To simulate the behavior of sand, a three-dimensional spherical discrete model YADE was developed at University of Grenoble (Kozicki and Donze, 2008) by taking advantage of the so-called soft-particle approach (i.e. the model allows for particle deformation which is modeled as an overlap of particles). A dynamic behavior of the discrete system is solved numerically using a force–displacement Lagrangian approach and tracks the positions, velocities, and accelerations of each particle individually. It uses an explicit finite difference algorithm assuming that velocities and

Table 1
Microscopic material parameters for discrete simulations of earth pressure problems.

Material parameter	Value
Modulus of elasticity of grain contact E_c [GPa]	30
Poisson's ratio of grain contact υ_c [−]	0.3
Grain size [mm]	0.2–0.8, 0.7–1.3, 2.0–8.0
Mean grain diameter d_{50} [mm]	0.5–5.0
Normal grain stiffness K_n [kPa]	$7.5 \times 10^3 (d_{50} = 0.5$ mm)
	$1.5 \times 10^4 (d_{50} = 1.0$ mm)
	$7.5 \times 10^4 (d_{50} = 5.0$ mm)
[1] Tangential grain stiffness K_s [kPa]	$2.25 \times 10^3 (d_{50} = 0.5$ mm)
	$4.50 \times 10^3 (d_{50} = 1.0$ mm)
	$2.25 \times 10^4 (d_{50} = 5.0$ mm)
Inter-particle friction angle μ [°]	30
Rolling stiffness coefficient β [−]	0.15
Moment limit coefficient η [−]	1.0
Initial void ratio e_0 [−]	0.63
Mass density ρ [kNs^2/m]	2.6
Damping coefficient α [−]	0.3

accelerations are constant in each time step. To calculate forces acting in particle–particle or particle–wall contacts, a particle interaction model is assumed in which the forces are typically subdivided into normal and tangential components. The total forces and moments acting on each particle are summed. Next, the problem is reduced to the integration of Newton's equations of motion for both translational and rotational degrees of freedom. As the results, the accelerations of each particle are obtained. The time step is incremented and accelerations are integrated over time to determine updated particle velocities and positions. To maintain the numerical stability of the method and to obtain a

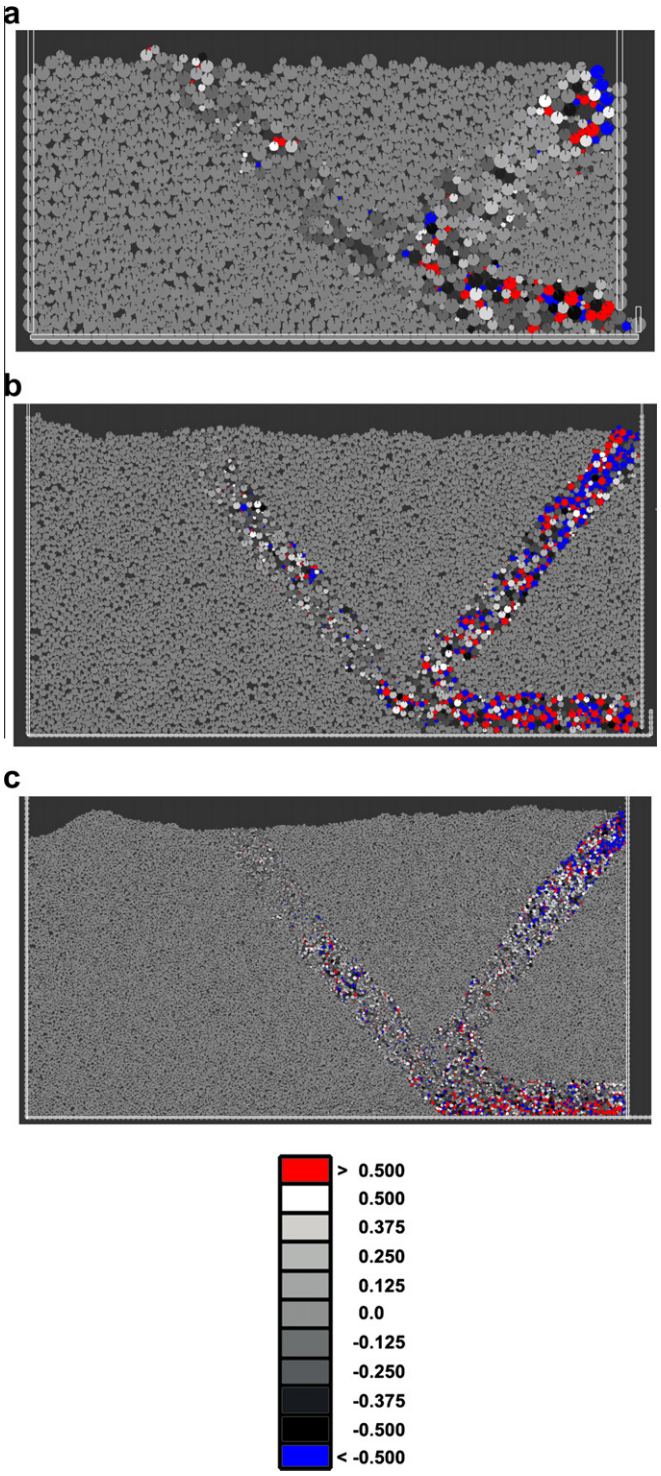

Fig. 11. Deformed granular body with distribution of rotation for initially dense sand from discrete simulations during passive earth pressure with translating wall: (a) $d_{50} = 5$ mm, (b) $d_{50} = 1$ mm and (c) $d_{50} = 0.5$ mm ($u/h = 0.05$, $e_o = 0.63$, $E_c = 30$ GPa, $\upsilon_c = 0.3$, $\mu = 30°$, $\eta = 1.0$, $\beta = 0.15$) (values of grain rotation in arc measure are expressed by scale).

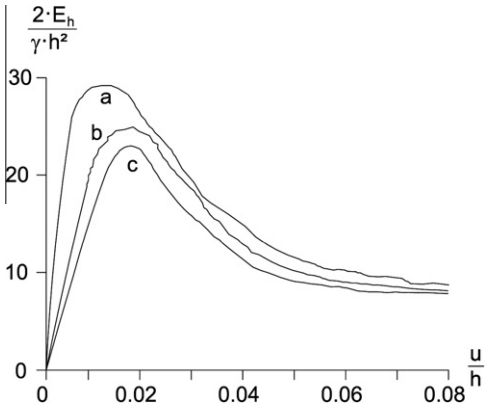

Fig. 12. Resultant normalized earth pressure force $2E_h/(\gamma h^2)$ versus normalized wall displacement u/h from discrete simulations during passive earth pressure with translating wall with different mean grain diameter d_{50}: (a) $d_{50} = 5$ mm, (b) $d_{50} = 1.0$ mm, (c) $d_{50} = 0.5$ mm (E_h – horizontal earth pressure force, γ– density, h – wall height, u – horizontal wall displacement) ($e_o = 0.63$, $E_c = 30$ GPa, $\upsilon_c = 0.3$, $\mu = 30°$, $\eta = 1.0$, $\beta = 0.15$).

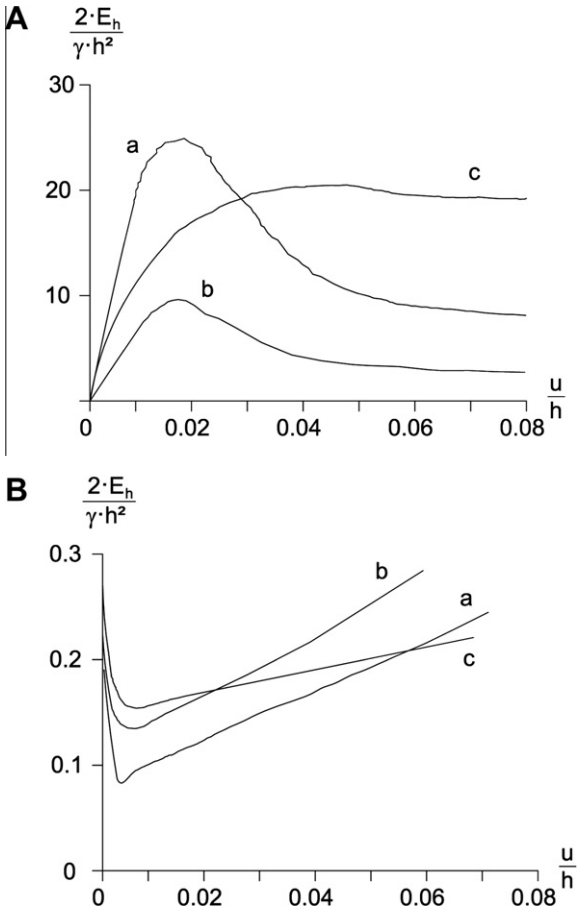

Fig. 13. Resultant normalized earth pressure force $2E_h/(\gamma h^2)$ versus normalized wall displacement u/h from DEM for: (A) passive case and (B) active case: (a) translating wall, (b) wall rotating around top, (c) wall rotating around toe (E_h – horizontal earth pressure force, γ – density, h – wall height, u – horizontal wall displacement) ($e_o = 0.63$, $d_{50} = 1$ mm, $E_c = 30$ GPa, $\upsilon_c = 0.3$, $\mu = 30°$, $\eta = 1.0$, $\beta = 0.15$).

quick convergence to a quasi-static state of equilibrium of the assembly of particles, damping forces have to be introduced (Cundall and Strack, 1979).

Discrete elements can have different geometries (Ketterhagen et al., 2008), but to keep a low calculation cost, usually the simplest spherical geometry is chosen (dealing with realistic shapes would lead to a prohibitive calculation cost). However, the spherical geometry is too idealized to accurately model phenomena exhibited by real granular materials. It has been shown that spherical particles have a smaller angle of repose and reduced shear strength as compared to non-spherical particles (Rothenburg and Bathurst, 1992). It is due to that the rotation is only resisted by frictional contacts with neighboring particles whereas for non-spherical particles the rotation tends to be inhibited by mechanical interlocking.

In the paper, spherical elements were used only. To simulate grain roughness, additional moments were introduced into a 3D model, which were transferred through contacts and resisted particle rotations (Kozicki and Donze, 2008). In this way, grains were

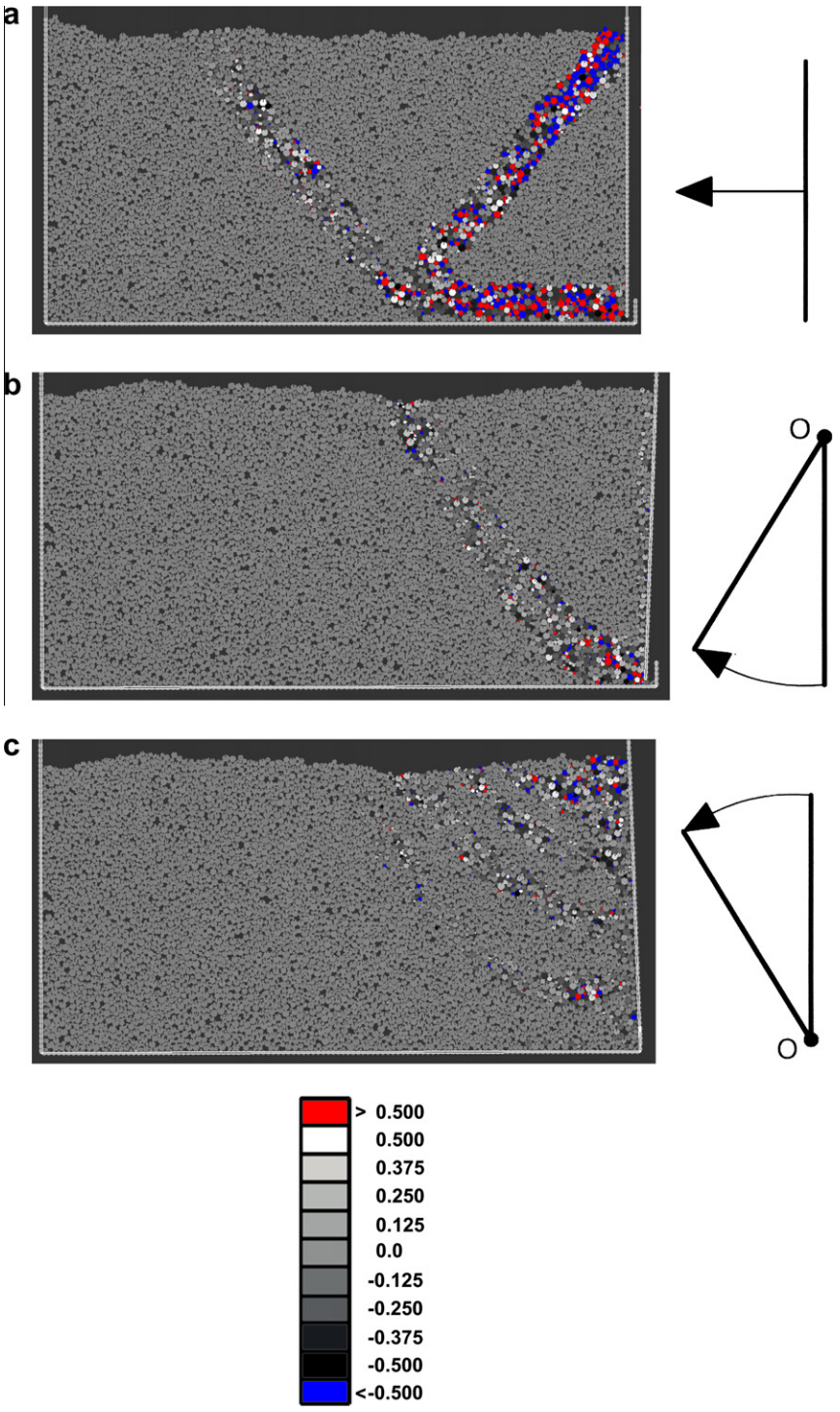

Fig. 14. Deformed granular body with distribution of rotation for initially dense sand from DEM (passive case, $u/h = 0.06$) for: (a) translating wall, (b) wall rotating around top, (c) wall rotating around toe ($e_o = 0.63$, $d_{50} = 1$ mm, $E_c = 30$ GPa, $\upsilon_c = 0.3$, $\mu = 30°$, $\eta = 1.0$, $\beta = 0.15$) (values of grain rotation in arc measure are expressed by scale).

in contact with their neighbors through a certain contact surface. The importance of rolling resistance on the contact behavior of granular bodies in 2D discrete simulations was shown among others by Iwashita and Oda (1998), Jiang et al. (2005) and Mohamed and Gutierrez (2010). The limitation of all discrete methods is a necessity of long computational time and a difficulty to validate it experimentally.

Fig. 8 presents two spherical discrete elements A and B in contact. The radii of two spheres are R_A and R_B. The positions of their centers are denoted by $\vec{X}_A$ and $\vec{X}_B$. During each time step, two spheres may remain in contact. The interaction force vector $\vec{F}$ represents the action of the element A on the element B and may be decomposed into a normal and tangential vector, respectively. Both forces are linked to displacements through the normal stiffness K_n and tangential stiffness K_s

$$\vec{F}_n = K_n U \vec{N}, \tag{1}$$

$$\vec{F}_s = \vec{F}_s + K_s \Delta \vec{X}_s, \tag{2}$$

where U is the penetration depth between elements, $\vec{N}$ denotes the normal vector at the contact point and $\Delta\vec{X}_s$ is the incremental tangential displacement. The tangential force $\vec{F}_s$ is obtained by

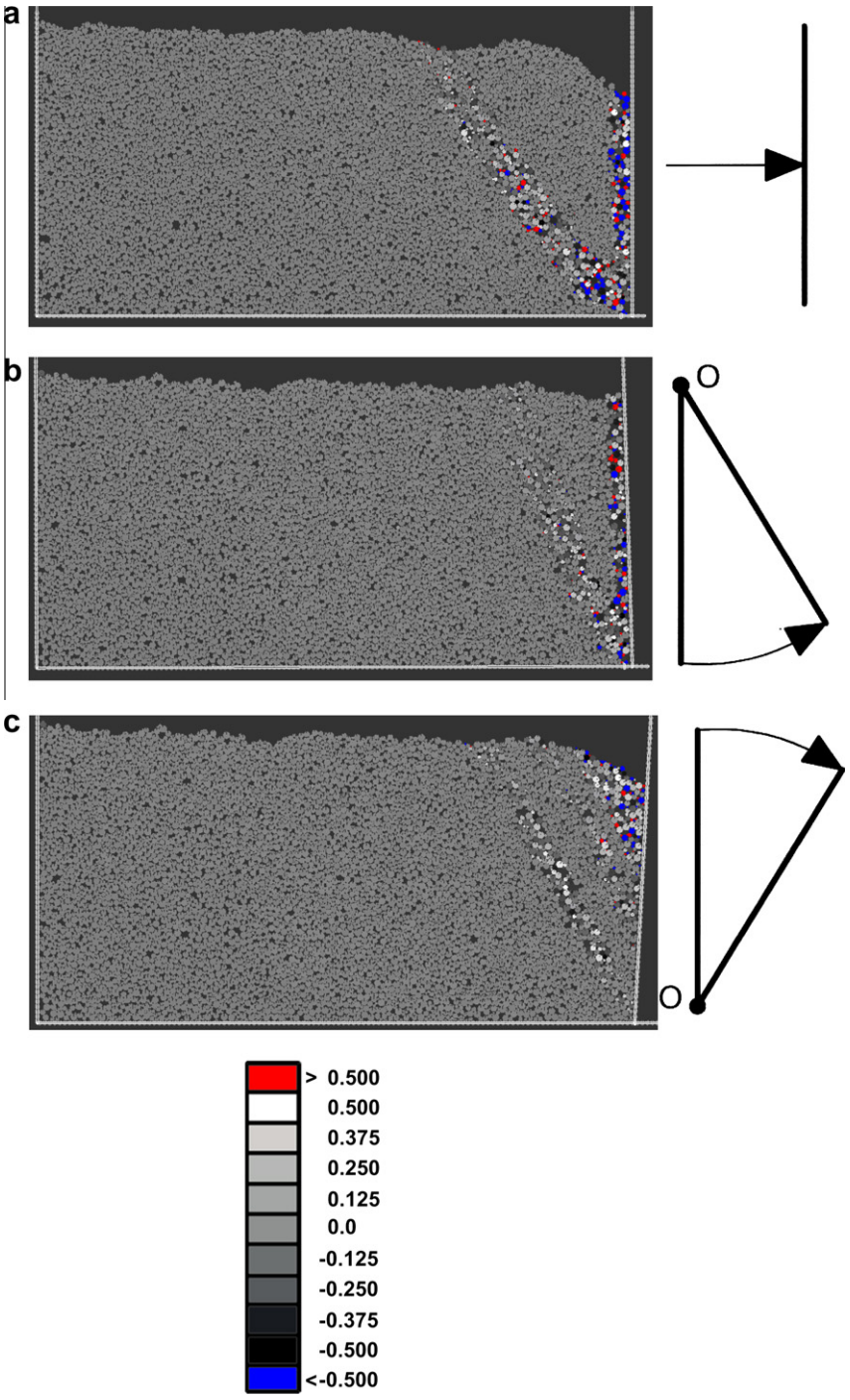

Fig. 15. Deformed granular body with distribution of rotation for initially dense sand from DEM (active case, $u/h = 0.06$): (a) translating wall, (b) wall rotating around top, (c) wall rotating around toe ($e_o = 0.63$, $d_{50} = 1$ mm, $E_c = 30$ GPa, $\nu_c = 0.3$, $\mu = 30°$, $\eta = 1.0$, $\beta = 0.15$) (values of grain rotation in arc measure are expressed by scale).

summing its increments. The stiffness parameters are calculated with the aid of the modulus of elasticity of the grain contact E_c and grain radii R (to determine the normal stiffness K_n) or a with the aid of the modulus of elasticity E_c and Poisson's ratio υ_c of the grain contact, and grain radii R (to determine the tangential stiffness K_s) of two neighbouring spheres, respectively:

$$K_n = E_c \frac{2R_A R_B}{R_A + R_B} \quad \text{and} \quad K_s = E_c \upsilon_c \frac{2R_A R_B}{R_A + R_B}. \tag{3}$$

If $R_A = R_B = R$, the stiffness parameters are equal to: $K_n = E_c R$ and $K_t = \upsilon_c E_c R$ (thus $K_n/K_t = 1/\upsilon_c$), respectively. Shearing starts at the contact point when the contact forces $\vec{F}_s$ and $\vec{F}_n$ satisfy a frictional Mohr–Coulomb equation

$$\|\vec{F}_s\| - \|\vec{F}_n\| \tan\mu \leqslant 0, \tag{4}$$

with μ as the inter-particle friction angle.

The program YADE differs from other DEM codes by the fact that contact moments between spheres are introduced to increase the rolling resistance. Due to that the real grain roughness can be simulated in 3D simulations. Only the normal force contributes to rolling resistance. The contact moment increments are calculated using the rolling stiffness K_r

$$\Delta M = K_r \Delta\vec{\omega}, \tag{5}$$

with

$$K_r = \beta K_s R_A R_B, \tag{6}$$

where β is the dimensionless rolling stiffness coefficient and $\Delta\vec{\omega}$ is the angular increment rotation between two spheres calculated as

$$\Delta\vec{\omega} = vec(\mathring{A}(\mathring{A}')^{-1}\mathring{B}'(\mathring{B})^{-1}), \tag{7}$$

where $\mathring{A}'$ and $\mathring{B}'$ are the unit quaternions representing orientations of the sphere A and sphere B when the contact was established, $\mathring{A}$ and $\mathring{B}$ are their current orientations and $vec(\bullet)$ is a function that converts rotation represented by a unit quaternion into a rotation vector. In turn, the dimensionless rolling coefficient η controls the limit of the rolling behavior

$$\|\vec{M}\| - \eta \frac{R_A + R_B}{2} \|\vec{F}_n\| \leqslant 0. \tag{8}$$

No forces and moments are transmitted when grains are separated. The assumed tangential, normal and rolling contact relationships in the model are demonstrated in Fig. 9a–c, respectively. To dissipate kinetic energy, a local non-viscous damping scheme was adopted (Cundall and Hart, 1992)

$$\vec{F}^k = \vec{F}^k - \alpha \cdot sgn(\vec{V}^k)|\vec{F}^k|, \tag{9}$$

$$\vec{M}^k = \vec{M}^k - \alpha \cdot sgn(\vec{\omega}^k)|\vec{M}^k|. \tag{10}$$

A positive numerical damping coefficient α is smaller than 1 ($sgn(\bullet)$ returns the sign of the argument). The equations are separately applied to each kth component of a 3D vector. In general, the damping parameter α can be different for each translational and rotational degree of freedom (but this is not the case in our quasi-static calculations).

The following five main local material parameters are needed for discrete simulations: E_c, υ_c, μ, β and η which were calibrated with corresponding triaxial laboratory test results with Karlsruhe sand (Wu, 1992). In addition, the particle radius R, particle density ρ and damping parameters α are required.

5. Calibration of discrete material parameters with triaxial test

The material sand parameters in our discrete model were calibrated with discrete simulations of a homogeneous triaxial test for cohesionless "Karlsruhe sand" (Widuliński et al., 2009), which were directly compared with the corresponding experimental results of several triaxial tests performed by Wu (1992) at Karlsruhe University. The calculations of a triaxial test were carried out with the real mean grain diameter of sand ($d_{50} = 0.5$ mm) using a linear size distribution curve (the radius of spheres varied between 0.2 mm and 0.8 mm). In numerical comparative simulations of a homogeneous triaxial test, a cubic granular specimen of $10 \times 10 \times 10$ cm^3 including about 10,000 spheres with contact moments was used. The spheres were distributed at random. The test was modeled using confining smooth rigid wall elements (without inducing shear localization). Isotropic compression took place under gravity free conditions. The top and bottom boundaries moved vertically as loading platens under strain-controlled conditions to simulate the confining pressure p. The initial density of sand was obtained using a radius expansion method based on a Weibull distribution. In this method, the inter-particle friction was assumed to be zero and gravity was varied to obtain a different initial density caused by grain overlapping (thus, it was possible to exactly reproduce the experimental sand density).

Fig. 10A and B shows a direct comparison between discrete and experimental results (Wu, 1992) with initially dense Karlsruhe sand ($e_o = 0.53$, $d_{50} = 0.5$ mm) at confining pressure $p = 200$ kPa up to $\varepsilon_1 = 12\%$ (with the following discrete material parameters: $E_c = 30$ GPa, $\upsilon_c = 0.3$, $\mu = 30°$, $\eta = 1.0$ and $\beta = 0.15$, $\rho = 2.6$ kNs^2/m, $\alpha = 0.3$). The both experimental curves (global axial normal stress versus global axial strain and global volumetric strain versus global axial strain) are very well reproduced. The calculated maximum internal friction angle, $\phi = 42.3°$, compares well with the experimental value of $\phi = 43.7°$ (Wu, 1992). The calculated dilatancy angle $\psi = 27.1°$ and modulus of elasticity $E = 101$ MPa are also in a satisfactory agreement with experimental outcomes of $\psi = 28.5°$ and $E = 104$ MPa. The other calculations show (Widuliński et al., 2009) that the local friction angle μ has a strong effect on both the peak stress and dilatancy angle, but an insignificant effect on the residual deviatoric stress. An increase of μ causes obviously the growth of ϕ^p and ψ. The rolling stiffness coefficient has a very strong effect on the entire stress–strain curve and a small effect on volume changes (the higher the parameter β, the greater is the

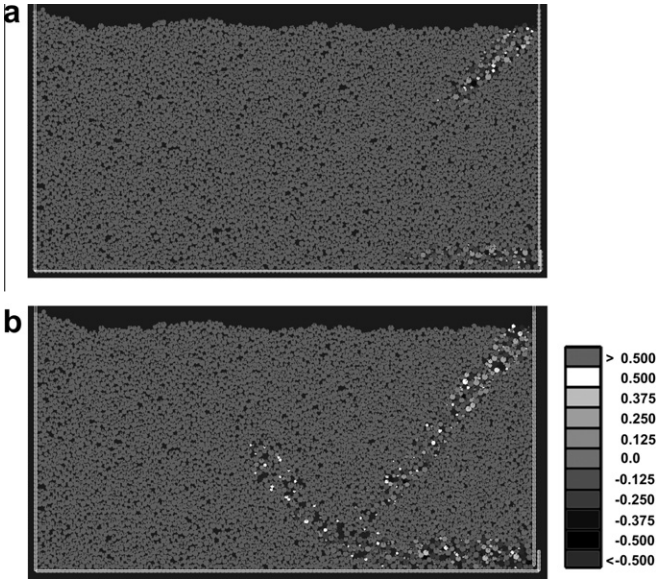

Fig. 16. Deformed granular body with distribution of rotation for initially dense sand from DEM at the beginning of passive earth pressure with translating wall: (a) $u/h = 0.01$, (b) $u/h = 0.02$ ($e_o = 0.63$, $d_{50} = 1$ mm, $E_c = 30$ GPa, $\upsilon_c = 0.3$, $\mu = 30°$, $\eta = 1.0$, $\beta = 0.15$).

mobilized global internal friction angle). The moment limit coefficient η has a pronounced influence on the stress–strain curve up to the residual state but an insignificant effect on volume changes (the higher the coefficient η, the greater is the peak global friction angle). The global modulus of elasticity and Poisson's ratio of sand grow with increasing E_c. Table 1 includes the material parameters assumed in further discrete simulations of earth pressures. The numerical damping was $\alpha = 0.3$ for each translational and rotational degree of freedom (its effect on our quasi-static results was negligible).

6. DEM results of earth pressure problem

The plane strain discrete calculations were performed with a sand body of a height of $H = 200$ mm and length of $L = 400$ mm to compare them directly with the FE results (Section 3). The height of the retaining wall located on the left-hand side of the granular body was assumed to be $h = 200$ mm. The vertical retaining wall and the bottom of the granular specimen were assumed to be stiff and very rough, i.e. there were no relative displacements along a vertical and bottom surface. The granular specimen depth was equal to the grain size.

6.1. Effect of mean grain diameter

First, to investigate the effect of a mean grain diameter of sand d_{50} on shear localization, the discrete calculations were carried with three different mean grain diameters d_{50}: 0.5 mm, 1.0 mm and 5 mm during a uniform horizontal passive translation u of the wall against the backfill. Five thousand spheres with different radii in the range 2–8 mm ($d_{50} = 5$ mm), 31,000 spheres with different radii of 0.7–1.3 mm ($d_{50} = 1.0$ mm) and 110,000 spheres with different radii of 0.2–0.8 mm ($d_{50} = 0.5$ mm) were assumed for calculations. The initial void ratio was about $e_o = 0.63$ (similar as in FE analyses). Fig. 11 presents the deformed granular body with the distribution of grain rotation ω for initially dense sand from DEM during passive earth pressure with translating wall. The values of grain rotations in the arc measure are expressed by

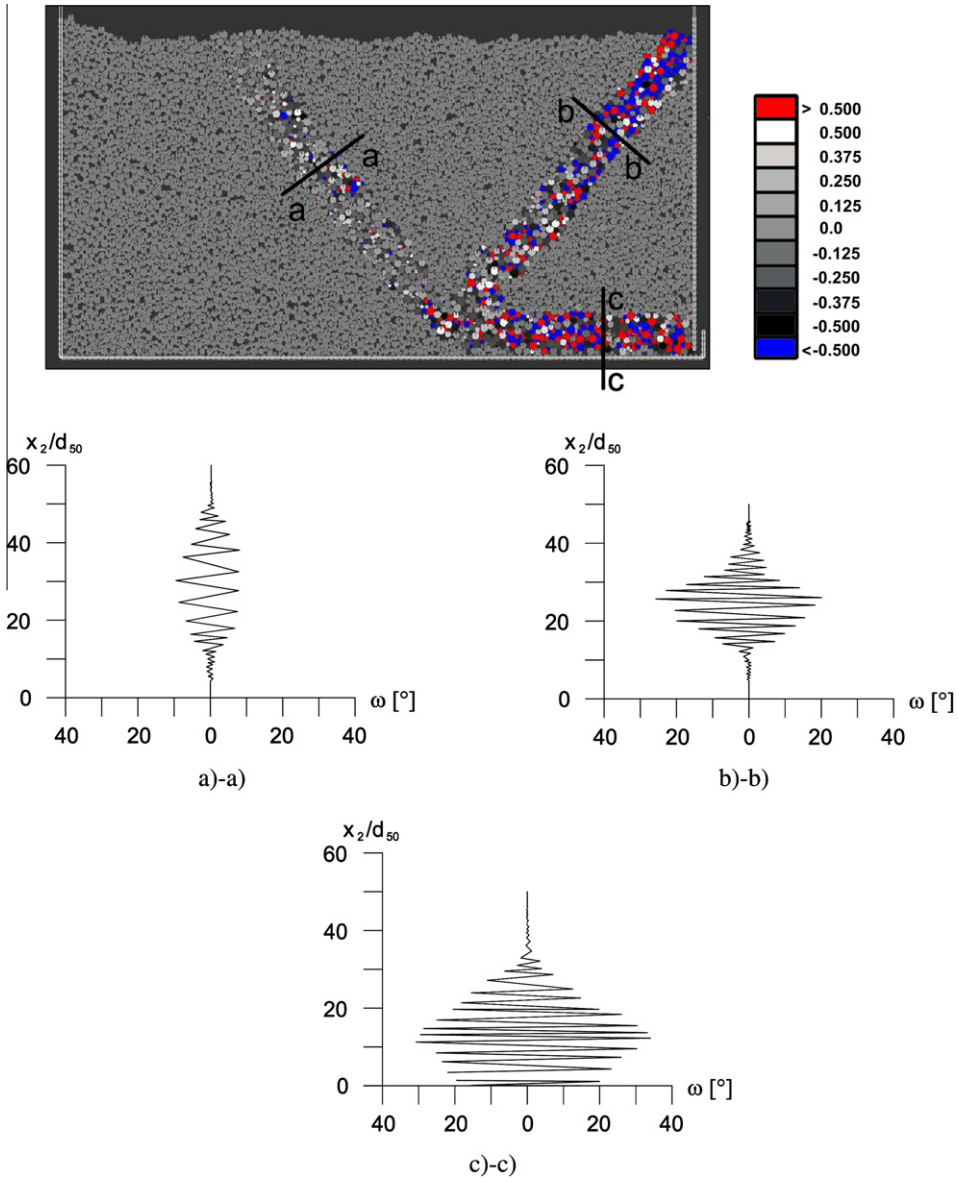

Fig. 17. Distribution of grain rotation ω[°] across shear zones at residual state during passive earth pressure with translating wall ($u/h = 0.05$, $e_o = 0.63$, $d_{50} = 1$ mm, $E_c = 30$ GPa, $\upsilon_c = 0.3$, $\mu = 30°$, $\eta = 1.0$, $\beta = 0.15$), x_2/d_{50} – normalized co-ordinate along shear zone width.

a scale attached. The gray color indicates no rotations ($\omega = 0$), the color between gray and white symbolizes rotations in the right direction (positive rotation, i.e. $\omega \in 0.0–0.5$) and the color between gray and black symbolizes rotations in the left one (negative rotation, i.e. $\omega \in -0.5$ to 0.0). To clearly distinguish the limits of grain rotations, in addition two colors were introduced. The color above the white one denotes the grain rotation higher than 0.5 and the color below the black one denotes the grain rotation smaller than −0.5. The geometry of shear zones was similar independently of d_{50}. In turn, the width of shear zones (Fig. 11) and the load–displacement curve (Fig. 12) strongly depended upon d_{50} (the maximum earth pressure force obviously increased with increasing d_{50}). The thickness of the main curved shear zone was 35 mm ($7 \times d_{50}$) with $d_{50} = 5.0$ mm, 22 mm ($22 \times d_{50}$) with $d_{50} = 1.0$ mm and 18 mm ($36 \times d_{50}$) with $d_{50} = 0.5$ mm.

The computation time was about 24 days ($d_{50} = 0.5$ mm), 7 days ($d_{50} = 1.0$ mm) and 1 day ($d_{50} = 5$ mm) on PC 3.2 GHz.

6.2. Effect of wall movement type

The discrete simulations results for passive and active earth pressure problem are shown for initially dense sand ($e_o = 0.63$) in Figs. 13–15. To reduce the computation time, further simulations were solely carried out with $d_{50} = 1.0$ mm. Fig. 13 presents the evolution of the normalized horizontal earth pressure force $2E_h/(\gamma h^2)$ versus the normalized horizontal wall displacement u/h for three different active (Fig. 13A) and passive (Fig. 13B) wall movements. In the case of a rotating wall, the horizontal displacement u is related to the wall displacement of the bottom point (wall rotating about the top) or top point (wall rotating around the bottom). In turn, the deformed granular body with the distribution of grain rotations is demonstrated in Fig. 14 (passive case) and Fig. 15 (active case).

The evolution of the horizontal earth pressure force $2E_h/(\gamma h^2)$ against the wall displacement is very similar as in FE calculations (Fig. 5). The maximum normalized passive horizontal forces $2E_h/\gamma h^2$ are between 9 and 25 (in FEM: $2E_h/\gamma h^2 = 12–31$, respectively), and the minimum normalized active earth pressure forces $2E_h/\gamma h^2$ lie between 0.08 and 0.16 (in FEM: $2E_h/\gamma h^2 = 0.10–0.16$, respectively). In turn, the calculated minimum (residual) earth pressure coefficients are about 3–18 in a passive case (in FEM: $2E_h/\gamma h^2 = 4–20$, respectively).

The pattern of shear zones in DEM simulations on the basis of grain rotations (Figs. 14 and 15) is similar as in FE calculations (Figs. 6 and 7) and experiments (Figs. 1–4). However, some discrepancies exist. For the passive wall translation (Fig. 14a), in contrast to FE-calculations (Fig. 6a) and experiments recorded by X-rays (Fig. 1a), one radial zone (as in experiments with DIC,

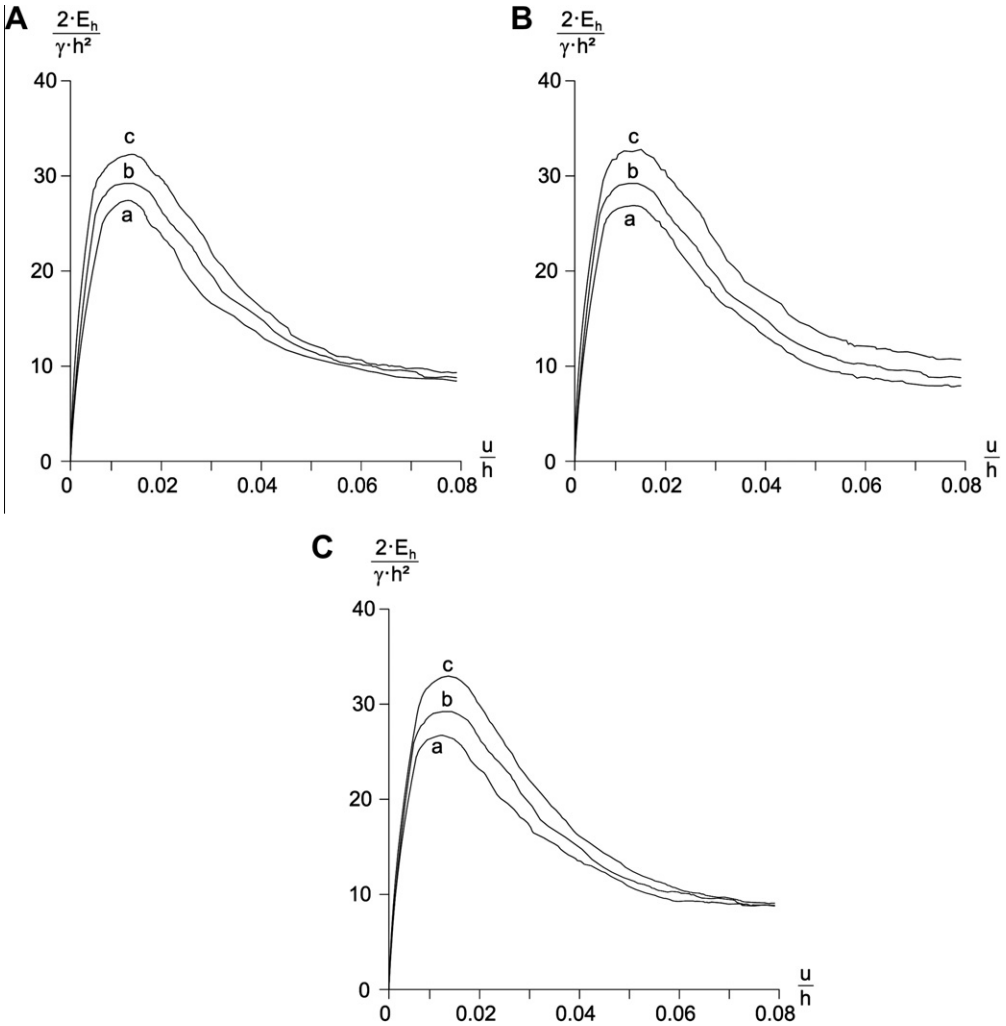

Fig. 18. Effect of micro-mechanical parameters in discrete simulations on resultant normalized earth pressure force $2E_h/(\gamma h^2)$ versus normalized wall displacement u/h from DEM (passive wall translation): (A) effect of μ (a) $\mu = 20°$, (b) $\mu = 30°$, (c) $\mu = 40°$, (B) effect of β (a) $\beta = 0.15$, (b) $\beta = 1.0$, (c) $\beta = 3.0$ and (C) effect of η (a) $\eta = 0.15$, (b) $\eta = 1.0$, (c) $\eta = 3.0$ (with $e_o = 0.63$, $d_{50} = 5$ mm, $E_c = 30$ GPa).

Fig. 3a) was obtained instead of two. In addition, secondary shear zones were not numerically obtained. The shear zones from discrete simulation are straighter than these from the FEM (during wall rotation around the toe). The differences between calculations and experiments are probably due to the fact that different sand was used in laboratory tests and in FE and DE analyses and due to a too small deformation range assumed in numerical calculations.

A horizontal shear zone and a radial shear zone develop first at the beginning of the passive wall translation (Fig. 16a). The material starts to generate grain rotations there. Next, a shear zone (starting from the wall base) curves upwards (Fig. 16b). At the same time, it is reached by a radial shear zone. The thickness of a shear zone reaching a top boundary surface is about $22 \times d_{50}$(d_{50} = 1.0 mm) with the inclination of 43° to the horizontal (in FEM: $30 \times d_{50}$ with d_{50} = 0.5 mm and 40°, respectively) and of a radial shear zone is also about $22 \times d_{50}$ with d_{50} = 1.0 mm (Fig. 16). In the case of the passive wall rotation around the top, the thickness of a curved shear zone is $25 \times d_{50}$ (the thickness of a curved shear zone from FEM was $25 \times d_{50}$ with d_{50} = 0.5 mm). The thickness of parallel shear zones during the passive wall rotation around the bottom is about $(15–18) \times d_{50}$ with d_{50} = 1.0 mm (in FEM the thickness was about $15 \times d_{50}$ with d_{50} = 0.5 mm). Their mean inclination against the bottom is 43°.

In the case of the active wall movement, the thickness of the interior shear zones is $25 \times d_{50}$ (wall translation, wall rotation around the top) and $(15–18) \times d_{50}$ (wall rotation around the toe), respectively (with d_{50} = 1.0 mm). The shear zone inclination to the horizontal is 58° (wall translation), 60° (wall rotation about the top) and 62° (wall rotation about the toe), respectively. In FEM, the thickness of the interior shear zones was $32.5 \times d_{50}$ (wall translation) $27.5 \times d_{50}$ (wall rotation around the top) $25 \times d_{50}$ (wall rotation around the toe), respectively (with d_{50} = 0.5 mm), and the shear zone inclination into the horizontal was 50° (wall translation), 60° (wall rotation about the top) and 60° (wall rotation about the toe), respectively.

The maximum grain rotation in the shear zones is about ±(15°–35°) at the residual state during passive wall translation (Fig. 17). It is obviously higher in shear zones which form earlier

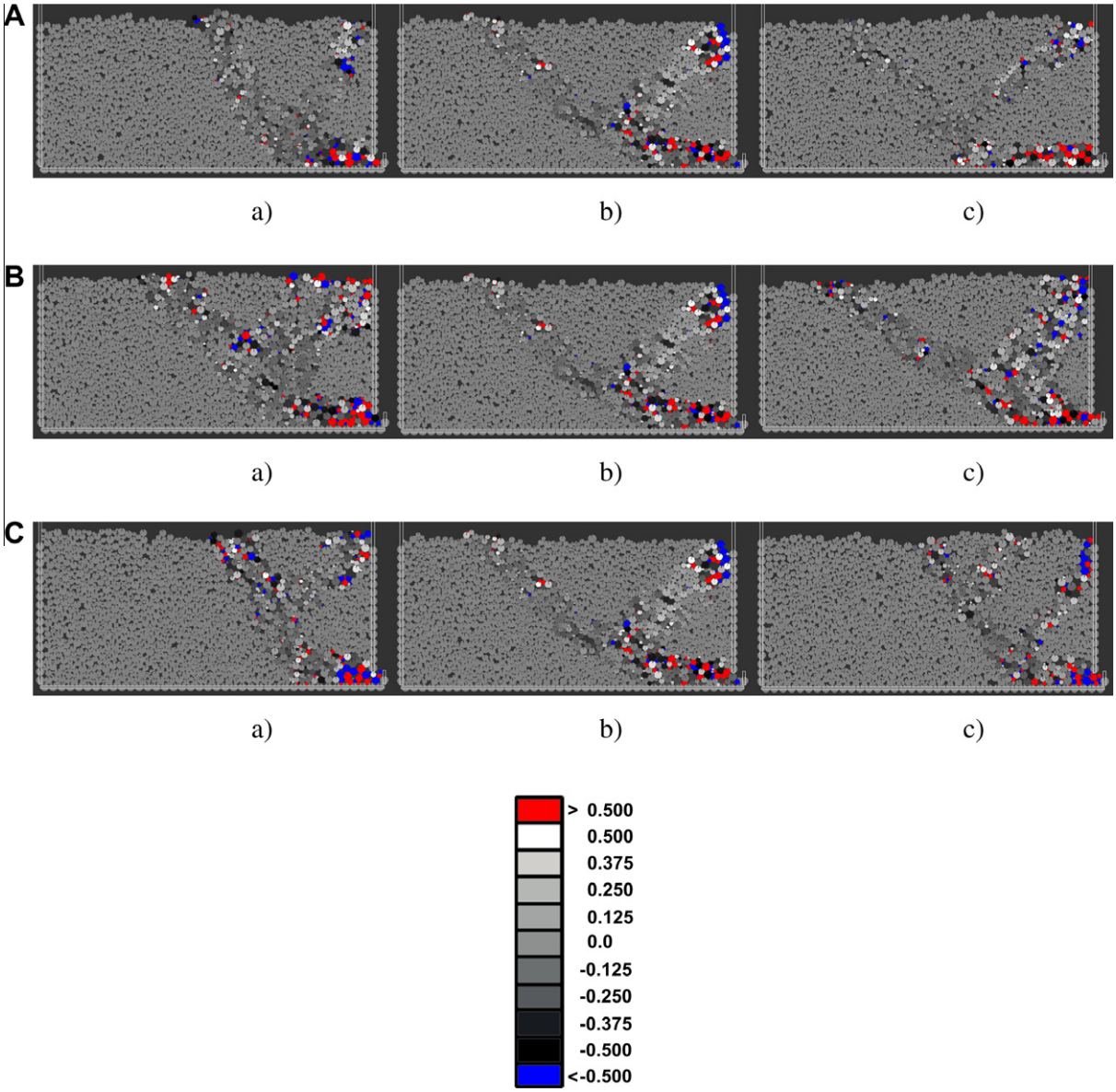

Fig. 19. Effect of micro-mechanical parameters in discrete simulations on deformation field (passive wall translation): (A) effect of μ (a) μ = 20°, (b) μ = 30°, (c) μ = 40°, (B) effect of β (a) β = 0.15, (b) β = 1.0, (c) β = 3.0 and (C) effect of η (a) η = 0.15, (b) η = 1.0, (c) η = 3.0 (with e_o = 0.63, d_{50} = 5 mm, E_c = 30 GPa) (values of grain rotation in arc measure are expressed by scale).

(e.g. in a horizontal shear zone at the bottom). In turn, the resultant grain rotation in the middle of the radial shear zone from the area $5d_{50} \times 5d_{50}$ is about 10° (and is approximately equal to the maximum Cosserat rotation in FE calculations Tejchman et al., 2007).

6.3. Effect of micro-mechanical parameters

Figs. 18 and 19 demonstrate the effect of micro-mechanical parameters on the geometry of shear zones and load–displacement curve during passive wall translation (with a high mean grain diameter d_{50} = 5 mm).

The maximum horizontal passive force on the wall grows with increasing parameters μ, β and η. In turn, the residual horizontal passive force depends on the parameter β only (it grows with increasing β). The maximum horizontal passive force on the wall increases by: 15% (if the inter-particle friction μ increases from μ = 20° up to μ = 40°), 20% (if the rolling stiffness coefficient β increases from β = 0.15 up to β = 0.30) and 20% (if the limit rolling coefficient η increases from η = 0.15 up to η = 0.30). In turn, the residual horizontal passive force on the wall increases by 40%, if the rolling stiffness coefficient β increases from β = 0.15 up to β = 0.30.

When the inter-particle friction μ is small, the main inclined shear zone is more curved and the radial zone is steeper. A larger stiffness parameter β contributes to that, a radial shear zone is steeper and the inclination of the main shear zone to the horizontal is smaller. If the rolling parameter η is high, an additional shear zone parallel to the radial zone is obtained.

6.4. Internal work, external work and dissipation

Figs. 20 and 21 show the calculated internal work, external work and dissipation in initially dense sand specimen of Fig. 11b during passive wall translation (d_{50} = 1.0 mm). The internal work δU was done by contact tangential forces on tangential displacements, contact normal forces on penetration depths and contact moments on angular rotations. The external work δW was done by the external horizontal force on the horizontal wall displacement. The total dissipation δD was calculated from the difference between the external work done on the assembly and internal work done by contact forces and moments.

The evolution of three components of the internal work (Fig. 21) is similar to the evolution of the horizontal wall force (Fig. 7). The normal contact forces, tangential contact forces and contact moments increase up to the peak, indicate softening and reach their asymptotes. The largest internal work at peak was performed by contact normal forces (45% of the total work) and contact tangential forces (40% of the total work) and the smallest one by contact moments (15% of the total work). In the residual state, the work performed by normal and tangential contact forces was similar and the work performed by contact moments was about 3 times smaller than the remaining ones.

The total dissipation in the granular specimen during deformation was about 25% at peak and 10% at the residual state, respectively (as compared to the total external work) (Fig. 20).

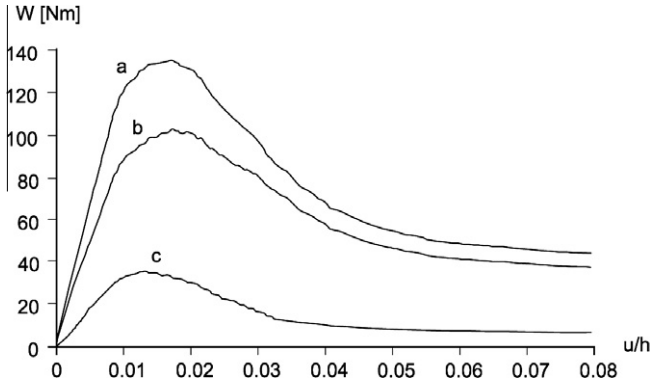

Fig. 20. Passive wall translation: (a) external work, (b) internal work and (c) dissipation from discrete simulations (d_{50} = 1.0 mm).

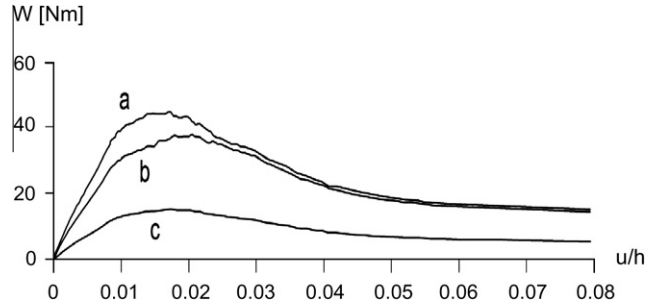

Fig. 21. Internal work done by: (a) normal contact forces, (b) tangential contact forces and (c) contact moments and during passive wall translation from discrete simulations (d_{50} = 1.0 mm).

7. Conclusions and future work

The numerical simulations of earth pressures behind a retaining wall show that a discrete element method is capable to reproduce the most important macroscopic properties of cohesionless granular materials without being necessary to describe the granular structure perfectly. The results confirm the previous discrete element results obtained for a single shear zone in granular bodies. Comparing discrete simulations with experimental tests and continuum calculations demonstrates that a discrete model realistically predicts experimental results of a complex pattern of shear zones in the interior of initially dense sand. Thus, it can be used to comprehensively study the mechanism of the initiation, growth and formation of multiple shear zones at the micro-level.

The following detailed conclusions can be also drawn:

- The geometry of shear zones depends strongly on the direction and type of the wall movement (passive or active, translation or rotation). The experimental patterns of shear zones were realistically reproduced in discrete calculations. The finite element and discrete results were very similar with respect to the geometry of shear zones and load–displacement curves.
- The largest passive earth pressures occur with the horizontal translation of the wall, they are smaller with the wall rotation around the bottom and again smaller with the wall rotation around the top. The smallest active earth pressures are created during wall translation, and the largest during wall rotation around the top.
- A mean grain size has a significant effect on a load–displacement diagram in DEM when shear localization is taken into account.
- The granular material tends to a critical state inside shear zones. The grain rotations are noticeable only in shear zones.
- The largest internal work in DEM simulations is performed by contact normal forces and the smallest one by contact moments.
- The maximum horizontal passive force on the wall grows with increasing micro-mechanical parameters μ, β and η. In turn, the residual horizontal passive force depends on β only.
- Conventional earth pressure mechanisms with slip surfaces are roughly reproduced. Realistic earth pressure coefficients can be obtained with actual values of internal friction angles only.

- A continuum model is more advantageous due to a possibility to simulate larger granular specimens with smaller grain sizes. The discrete model is still limited by computation time. However, a discrete model has a smaller amount of parameters to be calibrated.

Since shear zones entirely control a global post-peak response, it is necessary to understand the underlying nature of granular material behavior within shear zones to fully characterize the softening and critical state material response at the macro-level. In the next step, a detailed DE analysis of shear zones will be performed at the micro-level with respect to a micro-polar rotation (based on grain rotations), void ratio, stresses (based on normal and tangential contact forces) and couple stresses (based on contact moments). The DE results will be again compared with the FE outcomes. Thus, the results from discrete simulations will allow us to better understand a mechanism of the formation of a pattern of shear zones (depending upon the particle size, roughness and distribution) and to better calibrate a micro-polar hypoplastic constitutive model, wherein micro-polar rotations play a crucial role (what requires an accurate characterization of the micro-scale kinematics occurring in shear zones).

Acknowledgments

Research work has been carried out by the first three authors as a part of the project: "Innovative ways and effective methods of safety improvement and durability of buildings and transport infrastructure in the sustainable development" financed by the European Union.

References

Arthur, J.R.F., 1962. Strains and lateral force in sand. Ph.D. Thesis, University of Cambridge.
Bauer, E., 1996. Calibration of a comprehensive hypoplastic model for granular materials. Soils Found. 36 (1), 13–26.
Bransby, P.L., 1968. Stress and strain in sand caused by rotation of a model wall. Ph.D. Thesis, University of Cambridge.
Bransby, P.L., Milligan, G.W.E., 1975. Soil deformations near cantilever sheet pile walls. Geotechnique 25 (2), 175–195.
Cabalar, A.F., Cevik, A., 2010. Neuro-fuzzy based constitutive modeling of undrained response of Leighton Buzzard Sand mixtures. Expert Systems Appl. 37, 842–851.
Caquot, A., Kerisel, J., 1948. Tables for the Calculation of Passive Pressures, Active Pressures and Bearing Capacity of Foundations. Gauthier-Villars, Paris.
Christian, J.T., Hagmann, A.J., Marr, W.A., 1977. Incremental plasticity analysis of frictional soils. Int. J. Num. Anal. Meth. Geomech. 1, 343–375.
Coulomb, C.A., 1773. Essai sur une application des regles des maximis et minimis a quelques problemes de statique relatifs a l'architecture. Memoires de l'Academie Royale pres Divers Savants, vol. 7.
Cundall, P.A., Hart, R., 1992. Numerical modeling of discontinua. J. Eng. Comp. 9, 101–113.
Cundall, P.A., Strack, O.D.L., 1979. The distinct numerical model for granular assemblies. Geotechnique 29, 47–65.
Desrues, J., Viggiani, G., 2004. Strain localization in sand:overview of experiments in Grenoble using streo photogrammetry. Int. J. Numer. Anal. Methods Geomech. 28 (4), 279–321.
Gudehus, G., 1978. Engineering approximations for some stability problems in geomechanics. Advances in Analysis Geotechnical Instabilities, vol. 13. University Karlsruhe, pp. 1–24.
Gudehus, G., 1996a. A comprehensive constitutive equation for granular materials. Soils Found. 36 (1), 1–12.
Gudehus, G., 1996b. Erddruckermittlung. Grundbautaschenbuch, Teil 1. Ernst und Sohn.
Gudehus, G., Nübel, K., 2004. Evolution of shear bands in sand. Geotechnique 54 (3), 187–201.
Gudehus, G., Schwing, E., 1986. Standsicherheit historischer Stützwände. In: Internal Report of the Institute of Soil and Rock Mechanics. University Karlsruhe.
Han, C., Vardoulakis, Y., 1991. Plane strain compression experiments on water saturated fine-grained sand. Geotechnique 41, 49–78.
Herle, I., Gudehus, G., 1999. Determination of parameters of a hypoplastic constitutive model from properties of grain assemblies. Mech. Cohesive-Frictional Mater. 4 (5), 461–486.
Hicks, M.A., Yap, T.Y., Bakar, A.A., 2001. Adaptive and fixed mesh study of localisation in a strain-softening soil. In: Mühlhaus, H.B., Dyskin, A., Pasternak, E. (Eds.), Bifurcation and Localisation Theory in Geomechanics. Balkema, pp. 147–155.
Houlsby, G.T., Wroth, C.P., 1982. Direct solution of plasticity problems in soils by the method of characteristics. In: Proc. 4th Int. Conf. on Num. Meth. in Geomech., Edmonton, Canada, pp. 1059–1071.
Iwashita, K., Oda, M., 1998. Rolling resistance at contacts in simulation of shear band development by DEM. ASCE J. Eng. Mech. 124 (3), 285–292.
James, R.G., Bransby, P.L., 1971. A velocity field for some passive earth pressure problems. Geotechnique 21 (1), 61–83.
Jiang, M.J., Yu, H.-S., Harris, D.A., 2005. Novel discrete model for granular material incorporating rolling resistance. Comput. Geotech. 32 (5), 340–357.
Ketterhagen, W.R., Amende, M.T., Hancock, B.C., 2008. Process modeling in the pharmaceutical industry using the discrete element method. Pharm. Res. Dev.. doi:10.1002/jps.21466.
Kozicki, J., Donze, F.V., 2008. A new open-source software developed for numerical simulations using discrete modelling methods. Comput. Methods Appl. Mech. Eng. 197, 4429–4443.
Krasinski, A., 1998. Pile resistance in cohesionless soil depending on pile diameter, grain diameter and pressure (in polish). Ph.D. Thesis, Gdansk University of Technology, pp. 1–201.
Leśniewska, D., 2000. Shear band pattern formation in soil. In: Habilitation. Institute of Hydroengineering of the Polish Academy of Science.
Leśniewska, D., Mróz, Z., 2001. Study of evolution of shear band systems in sand retained by flexible wall. Int. J. Numer. Anal. Methods Geomech. 25, 909–932.
Lord, J.A., 1969. Stress and strains in an earth pressure problem. Ph.D. Thesis, University of Cambridge.
Lucia, J.B.A., 1966. Passive earth pressure and failure in sand. Research Report, University of Cambridge.
Luding, S., 2008. Cohesive, frictional powders: contact models for tension. Granular Matter 10 (4), 235–246.
Milligan, G.W.E., 1983. Soil deformations near anchored sheet-pile walls. Geotechnique 33 (1), 41–55.
Mohamed, A., Gutierrez, M., 2010. Comprehensive study of the effects of rolling resistance on the stress–strain and strain localization behavior of granular materials. Granular Matter 12, 527–541.
Mühlhaus, H.-B., 1990. Continuum models for layered and blocky rock. In: Hudson, J.A., Fairhurst, Ch. (Eds.), Comprehensive Rock Engineering, vol. 2. Pergamon, pp. 209–231.
Nakai, T., 1985. Analysis of earth pressure problems considering the influence of wall friction and wall deflection. In: Proc. Int. Conf. Num. Meth. Geomech. Nagoya, pp. 765–772.
Negre, R., 1959. Sur une methode approchee de la repatition des equilibre limite des massifs plans a faible frottement interne. C.R.A.S., Paris, pp. 3118–3120.
Niedostatkiewicz, M., 2003. Dynamic effects in silos (in Polish). Ph.D. Thesis, Gdańsk University of Technology, pp. 1–272.
Niedostatkiewicz, M., 2009. Application of X-ray Technique for Monitoring Deformation of Granular Materials During Earth Pressure Problems. Internal Report of Gdansk University of Technology.
Niedostatkiewicz, M., Leśniewska, D., Tejchman, J., 2010. Experimental analysis of shear zone patterns in sand for earth pressure problems using Particle Image Velocimetry. Strain. doi:10.1111/j.1475-1305.2010.00761.x2010.
Nübel, K., 2002. Experimental and numerical investigation of shear localisation in granular materials. Publication Series of the Institute of Soil and Rock Mechanics, vol. 62. University Karlsruhe.
Nübel, K., Huang, W., 2004. A study of localized deformation pattern in granular media. Comput. Methods Appl. Mech. Eng. 193, 2719–2743.
Oda, M., 1993. Micro-fabric and couple stress in shear bands of granular materials. In: Thornton, C. (Ed.), Powders and Grains, Rotterdam. Balkema, pp. 161–167.
Ord, A., Hibbs, B., Regenauer-Lieb, K., 2007. Shear band emergence in granular materials – a numerical study. Int. J. Numer. Anal. Methods Geomech. 31, 373–393.
Pasternak, E., Mühlhaus, H.-B., 2001. Cosserat continuum modelling of granulate materials. In: Valliappan, S., Khalili, N. (Eds.), Computational Mechanics – New Frontiers for New Millennium. Elsevier Science, pp. 1189–1194.
Pena, A.A., Lizcano, A., Alonso-Marroquin, F., Herrmann, H.J., 2008. Biaxial test simulations using a packing of polygonal particles. Int. J. Numer. Anal. Methods Geomech. 32, 143–160.
Potts, D.M., Fourie, A.B., 1984. The behaviour of a propped retaining wall: results of a numerical experiment. Geotechnique 34 (3), 383–404.
Rechenmacher, A.L., Finno, R.J., 2004. Digital image correlation to evaluate shear banding in dilative sands. Geotech. Testing J. 27 (1), 13–22.
Roscoe, K.H., 1970. The influence of strains in soil mechanics. Geotechnique 20 (2), 129–170.
Rothenburg, L., Bathurst, R.J., 1992. Micromechanical features of granular materials with planar elliptical particles. Geotechnique 42, 79–95.
Simpson, B., Wroth, C.P., 1972. Finite element computations for a model retaining wall in sand. In: Eisenstein, Z. (Ed.), Proc. Int. Conf. on Num. Meth. in Geomech. Edmonton 1982, pp. 85–93.
Skarżynski, L., Syroka, E., Tejchman, J., 2009. Measurements and calculations of the width of the fracture process zones on the surface of notched concrete beams. Strains. doi:10.1111/j.1475-1305.2008.00605.x.
Słomiński, C., Niedostatkiewicz, M., Tejchman, J., 2007. Application of particle image velocimetry (PIV) for deformation measurement during granular silo flow. Powder Technol. 173 (1), 1–18.
Smith, I., 1972. Stress and strain in a sand mass adjacent to a model wall. Ph.D. Thesis, University of Cambridge.

Sokolovski, V.V., 1965. Statics of Granular Media. Pergamon Press.
Szczepiński, W., 1974. Limit states and kinematics of granular materials (in Polish). PWN, Warszawa.
Tejchman, J., 2004. Influence of a characteristic length on shear zone formation in hypoplasticity with different enhancements. Comput. Geotech. 31 (8), 595–611.
Tejchman, J., 2008. FE modeling of shear localization in granular bodies with micro-polar hypoplasticity. In: Wu, Borja (Eds.), Springer Series in Geomechanics and Geoengineering. Springer Verlag, Berlin-Heidelberg.
Tejchman, J., Dembicki, E., 2001. Numerical analysis of active and passive earth pressures of granular soil on retaining walls (in polish), Inżynieria Morska and Geotechnika. J. Mar. Eng. nad Geotechnics 6, 365–368.
Tejchman, J., Górski, J., 2008. Computations of size effects in granular bodies within micro-polar hypoplasticity during plane strain compression. Int. J. Solids Struct. 45 (6), 1546–1569.
Tejchman, J., Gudehus, G., 2001. Shearing of a narrow granular strip with polar quantities. Int. J. Numer. Anal. Methods Geomech. 25, 1–18.
Tejchman, J., Wu, W., 2009. FE-investigations of non-coaxiality and stress-dilatancy rule in dilatant granular bodies within micro-polar hypoplasticity. Int. J. Numer. Anal. Methods Geomech. 33 (1), 117–142.
Tejchman, J., Bauer, E., Tantono, S.F., 2007. Influence of initial density of cohesionless soil on evolution of passive earth pressure. Acta Geotechnica 2 (1), 53–63.
Terzaghi, K., 1951. Mecanique theorique des sols. Dunod, Paris.
Thornton, C., Zhang, L., 2006. A numerical examination of shear banding and simple shear non-coaxial flow rules. Philos. Mag. 86 (21–22), 3425–3452.
Vardoulakis, I., 1980. Shear band inclination and shear modulus in biaxial tests. Int. J. Numer. Anal. Methods Geomech. 4 (2), 103–119.
Wang, C.C., 1970. A new representation theorem for isotropic functions. J. Rat. Mech. Anal. 36, 166–223.
White, D.J., Take, W.A., Bolton, M.D., 2003. Soil deformation measurements using particle image velocimetry (PIV) and photogrammetry. Geotechnique 53 (7), 619–631.
Widuliński, Ł., Kozicki, J., Tejchman, J., 2009. Numerical simulation of a triaxial test with sand using DEM. Arch. Hydro-Eng. Environ. Mech. 56 (3–4), 3–26.
Wu, W., 1992. Hypoplastizität als mathematisches Modell zum mechanischen Verhalten granularer Stoffe. In: Heft 129, Institute for Soil- and Rock-Mechanics. University of Karlsruhe.
Yoshida, T., Tatsuoka, F., Siddiquee, M.S.A., Kamegai, Y., 1995. Shear banding in sands observed in plane strain compression. In: Chambon et al. (Eds.), Localisation and Bifurcation Theory for Soils and Rocks. Balkema, pp. 165–179.
Ziegler, M., 1986. Berechnung des verschiebungsabhängigen Erddruckes in Sand. Ph.D. Thesis, Institute for Soil and Rock Mechanics, Karlsruhe University.